



CERN-EP-2022-266
28 November 2022

Multiplicity dependence of charged-particle production in pp, p–Pb, Xe–Xe and Pb–Pb collisions at the LHC

ALICE Collaboration*

Abstract

Multiplicity (N_{ch}) distributions and transverse momentum (p_{T}) spectra of inclusive primary charged particles in the kinematic range of $|\eta| < 0.8$ and $0.15 \text{ GeV}/c < p_{\text{T}} < 10 \text{ GeV}/c$ are reported for pp, p–Pb, Xe–Xe and Pb–Pb collisions at centre-of-mass energies per nucleon pair ranging from $\sqrt{s_{\text{NN}}} = 2.76 \text{ TeV}$ up to 13 TeV. A sequential two-dimensional unfolding procedure is used to extract the correlation between the transverse momentum of primary charged particles and the charged-particle multiplicity of the corresponding collision. This correlation sharply characterises important features of the final state of a collision and, therefore, can be used as a stringent test of theoretical models. The multiplicity distributions as well as the mean and standard deviation derived from the p_{T} spectra are compared to state-of-the-art model predictions. Providing these fundamental observables of bulk particle production consistently across a wide range of collision energies and system sizes can serve as an important input for tuning Monte Carlo event generators.

arXiv:2211.15326v3 [nucl-ex] 17 May 2024

1 Introduction

In high-energy nucleus–nucleus (AA) collisions, a hot and dense state of deconfined strongly-interacting matter, commonly denoted as the quark–gluon plasma, is formed [1]. This system undergoes hydrodynamic evolution [2–4] and exhibits hadron yields indicating chemical equilibrium [5, 6]. At low to intermediate transverse momentum (p_T), up to about a few GeV/ c , charged-particle production is influenced by the collective expansion (flow) of the system, reflected in the shapes of single-particle transverse-momentum spectra [7, 8] and multi-particle correlations [2]. It came as a major surprise that even small collision systems such as proton–proton (pp) and proton–nucleus (pA) collisions at Large Hadron Collider (LHC) energies exhibit features that can be attributed to collective expansion [9–17].

Multi-particle correlations measured in all collision systems, contain an imprint of the initial state of the colliding partners, characterised via their quark and gluon degrees of freedom, allowing the extraction of fundamental properties of the quark–gluon plasma [3, 4, 18]. Hydrodynamic-like (final-state) collective flow is increasingly part of the modelling of small collision systems [19, 20] in an interplay with initial-state phenomena (see reviews in Refs. [17, 21]). Such collision systems are usually modelled in the framework of the colour glass condensate (CGC) [22], where multi-particle production proceeds via the decay of colour flux tubes that stretch between two colliding hadrons in the longitudinal direction and are coherent in the transverse direction over a range that is inversely proportional to a saturation scale Q_s , which appears due to the non-linearity of parton evolution at high energies.

In the PYTHIA8 event generator [23], which describes a broad range of observables in pp collisions, the initial state is determined by parton distribution functions extracted from measurements. With increasing collision energy, the role of multi-parton interactions, i.e., when two or more distinct (hard) parton interactions occur within a pp collision, becomes more and more important [24]. The respective colour strings may cut each other or reconnect, which leads to a redistribution of energy from particle production to transverse momentum, and, therefore, a smaller number of particles but with higher average p_T . A phenomenon recently implemented in PYTHIA is the interaction between transversely-extended colour strings, exerting pressure on each other [25]. This produces effects similar to those resulting from final-state collective dynamics, akin to that of a long-lived quark–gluon medium. Recently, PYTHIA8 was extended with the Angantyr model for heavy-ion collisions [26], which uses a Glauber-based initial-state modelling with Gribov colour fluctuations to determine the number of pp sub-collisions. In current PYTHIA8 implementations with the Angantyr model, there is no colour reconnection between individual pp sub-collisions but between the multiple partonic interactions of the pp sub-collisions.

A broad range of observables is also described successfully in the EPOS family Monte Carlo (MC) event generators [27]. The initial state is realised in EPOS through a parton-based Gribov-Regge theory [27] which is a multiple scattering framework, recently augmented with the treatment of saturation effects [28]. While in EPOS3 [29], a full hydrodynamic evolution is included for the final state, in EPOS LHC [30] a parameterised hydrodynamic component of a small volume with high density of thermalised matter is used together with a dilute region, i.e. a core plus corona implementation. In both PYTHIA8 and EPOS LHC models, the respective parameters are tuned using the Run 1 data at the LHC [30, 31].

The mean transverse momentum, $\langle p_T \rangle$, of the charged-particle p_T spectrum and its correlation with the charged-particle multiplicity N_{ch} carry essential information on the underlying particle production mechanism. This has been studied by many experiments at hadron colliders in pp(\bar{p}) covering centre-of-mass energies from $\sqrt{s} = 31$ GeV up to 13 TeV [32–41] as well as in Xe–Xe [42] and Pb–Pb [8] collisions at $\sqrt{s_{\text{NN}}} = 5.44$ TeV and 5.02 TeV, respectively. All experiments observed an increase of $\langle p_T \rangle$ with N_{ch} in the central rapidity region, explained in the PYTHIA approach as a consequence of non-trivial colour reconnections (see discussion in Ref. [43]). While in the CGC approach $\langle p_T \rangle$ is a universal function of the ratio of the charged-particle multiplicity to the transverse area of the collision [44], in

the EPOS LHC model it is determined by the collective expansion [30]. For all collision systems, the $\langle p_T \rangle - N_{\text{ch}}$ correlation is a basic observable for tuning or calibrating the theoretical models [19], a simple observable which allows extracting fundamental properties of a deconfined quark–gluon medium [4].

As bulk production at the LHC is driven by a complex interplay of soft and hard QCD processes, the endeavour to find a consistent model description for particle production in all collision systems has not been concluded yet. At the LHC, a large amount of data was recorded in Run 1 and Run 2, covering different collision systems from pp to heavy-ion collisions at various centre-of-mass energies, which allows a detailed study of particle production over a wide range of charged-particle multiplicity. This Letter presents a measurement of the charged-particle multiplicity distributions and the corresponding transverse momentum spectra as a function of N_{ch} in pp, p–Pb, Xe–Xe and Pb–Pb collisions at centre-of-mass energies per nucleon pair ranging from $\sqrt{s_{\text{NN}}} = 2.76$ TeV up to 13 TeV. From these spectra, the mean $\langle p_T \rangle$ and standard deviation $\sigma(p_T) = \sqrt{\langle (p_T - \langle p_T \rangle)^2 \rangle}$ within $0.15 \text{ GeV}/c < p_T < 10 \text{ GeV}/c$ are extracted. The comprehensive set of measurements presented in this Letter can serve as a high-precision input for tuning phenomenological models towards the goal of understanding particle production in the non-perturbative regime of QCD and its transition to the perturbative regime.

This Letter is structured as follows. Section 2 briefly describes the experimental setup. In Section 3, the data used for this analysis and a detailed description of the analysis procedure are presented. Results are discussed in Section 4, and a summary is given in Section 5.

2 Experimental setup

The measurements reported in this Letter were obtained with ALICE at the Large Hadron Collider. In the following, the detectors relevant for this work are discussed briefly. A more detailed description of the ALICE apparatus in its configurations of LHC Run 1 and Run 2 can be found in Refs. [45, 46].

The present analysis is based on tracking information from the Inner Tracking System (ITS) [47] and the Time Projection Chamber (TPC) [48]. Both detectors are located within a large solenoidal magnet which provides a nominal field strength of 0.5 T for all of the data taking periods analysed in this work, except for the Xe–Xe data taking, where the magnetic field was reduced to 0.2 T in order to extend the kinematic acceptance of the detector to lower transverse momentum. The ITS is comprised of six cylindrical layers of silicon detectors with radii between 3.9 cm and 43 cm. Its two innermost layers are equipped with silicon pixel detectors (SPD), the two intermediate layers consist of silicon drift detectors (SDD), and the two outermost layers are made of double-sided silicon strip detectors (SSD). The large cylindrical TPC has an active radial range from about 85 cm to 250 cm and an overall length along the beam direction of about 500 cm. It covers the full azimuth in the pseudorapidity range $|\eta| < 0.9$ and provides track reconstruction with up to 159 space points along the trajectory of a charged particle as well as particle identification via the measurement of specific energy loss dE/dx .

The V0 detector, which consists of two scintillator arrays covering the pseudorapidity ranges of $2.8 < \eta < 5.1$ (V0A) and $-3.7 < \eta < -1.7$ (V0C), is used for triggering on hadronic collisions and multiplicity measurements at forward rapidity [8, 49]. Contamination from electromagnetic interactions in Pb–Pb and Xe–Xe collisions was strongly suppressed using signals from two neutron-Zero-Degree Calorimeters (ZDC), positioned on both sides of the interaction point at 114.0 m distance, see [46] for details.

3 Analysis procedure

This analysis aims to obtain the correlation between primary charged-particle p_T spectra and their corresponding event multiplicities N_{ch} , both defined consistently in the kinematic range $|\eta| < 0.8$ and $0.15 \text{ GeV}/c < p_T < 10 \text{ GeV}/c$. This kinematic selection ensures optimal momentum resolution and homogeneous tracking efficiency over the entire range. In addition, the multiplicity distributions for $N_{\text{ch}} > 0$

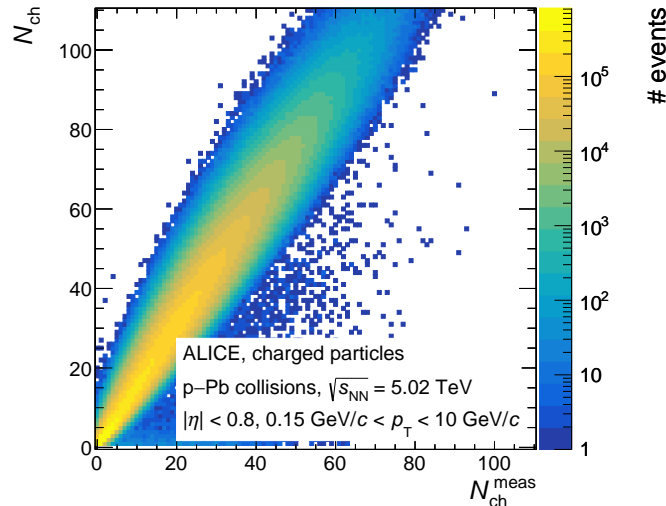


Figure 1: Multiplicity correlation matrix for p–Pb collisions at $\sqrt{s_{\text{NN}}} = 5.02$ TeV.

events are reported. For each collision, the number of reconstructed tracks selected for the analysis provides an experimental measure ($N_{\text{ch}}^{\text{meas}}$) for its multiplicity. Due to detector acceptance and reconstruction efficiency, this measured track multiplicity $N_{\text{ch}}^{\text{meas}}$ is different from the actual number of primary charged particles (N_{ch}) produced in the kinematic region under study. Secondary particles from weak decays or from interactions with the detector material as well as tracks that are smeared into the acceptance (i.e. from $|\eta| \geq 0.8$ and $p_{\text{T}} \leq 0.15$ GeV/ c , $p_{\text{T}} \geq 10$ GeV/ c) remaining in the sample of selected tracks further contribute to the measured p_{T} spectra and consequently to the measured track multiplicity. The event-by-event fluctuations of reconstruction efficiency and contamination effects lead to a rather broad correlation between N_{ch} and $N_{\text{ch}}^{\text{meas}}$ that is shown in Fig. 1 for an example data set. As a result, the transverse momentum spectrum associated to a given $N_{\text{ch}}^{\text{meas}}$ value carries contributions on particle production from a range of different N_{ch} values. In addition, the finite resolution of the transverse momentum measurement itself results in a (small) smearing of the measured transverse momentum $p_{\text{T}}^{\text{meas}}$. The correct correlation between the collision-characteristic N_{ch} value and its corresponding p_{T} distribution can be extracted by unfolding the measured quantities.

Data sets and event selection The data analysed in this work were collected between 2010 and 2018 during the LHC Run 1 and Run 2 data-taking periods. They comprise pp, p–Pb, Xe–Xe, and Pb–Pb collisions at centre-of-mass energies per nucleon pair ranging from $\sqrt{s_{\text{NN}}} = 2.76$ up to 13 TeV. Hadronic collisions were selected with two different minimum-bias (MB) interaction triggers. In Run 1, a single hit in either of V0A or V0C detectors or in the SPD was required (denoted as V0OR) in coincidence with a crossing of two particle bunches in the LHC at the nominal ALICE interaction point. For the Run 2 data taking period, a signal in both V0A and V0C was necessary to fulfil the MB trigger condition (denoted V0AND). Therefore, the former is also sensitive to single diffractive pp events while the latter almost exclusively selects non-single diffractive interactions. The offline event selection (for details see Ref. [8, 49]) is optimised to reject beam-induced background and pileup collisions. Events with no reconstructed vertex and those with poor vertex resolution are rejected. Both the trigger efficiency and the vertex requirements affect mostly low multiplicity events. To ensure full pseudorapidity coverage of the tracking detectors (in particular by the inner ITS layers) and therefore avoid a possible asymmetry in the kinematic selection of the tracks, all collisions are required to have their reconstructed primary vertex located within $|V_z^{\text{meas}}| < 10$ cm along the beam direction with respect to the nominal interaction point. Table 1 shows an overview of the data sets and their corresponding number of events selected for this analysis. In order to have comparable results regardless of the trigger setup and event selections,

Table 1: Overview of the analysed data sets. The definitions of the two MB triggers are explained in the text.

	$\sqrt{s_{NN}}$ (TeV)	year	MB trigger	no. events analysed (M)
pp	2.76	2011	V0OR	48
	5.02	2017	V0AND	316
	7	2010	V0OR	129
	8	2012	V0AND	26
	13	2016	V0AND	180
p-Pb	5.02	2016	V0AND	309
	8.16	2016	V0AND	15
Xe-Xe	5.44	2017	V0AND	1
Pb-Pb	2.76	2010	V0OR	19
	5.02	2015, 2018	V0AND	239

all measurements presented in this Letter are corrected using Monte Carlo simulations such that they represent collisions with at least one charged particle produced in the kinematic range $|\eta| < 0.8$ and $0.15 \text{ GeV}/c < p_T < 10 \text{ GeV}/c$. For this event class, the possible bias originating from Monte Carlo event generators for very low N_{ch} values (partially originating from diffractive or electromagnetic events) is minimal.

Track selection A primary charged particle [50] is defined as a charged particle with a mean proper lifetime τ larger than $1 \text{ cm}/c$, which is either produced directly in the interaction or from decays of particles with τ smaller than $1 \text{ cm}/c$, excluding particles produced in interactions with the detector material. Charged-particle trajectories are reconstructed using both the ITS and TPC detectors. In order to select only tracks with good p_T resolution for analysis, a minimal length in the active detector volume as well as a good agreement of the final track parameterisation with its comprising space points are required. The contamination of the track sample with weakly decaying particles, secondary particles from interactions of primary particles with the detector material and from pileup events is significantly reduced by selecting only tracks originating from a location close to the primary interaction vertex. In previous ALICE publications [8, 42] those selection criteria were studied in great detail and optimised for best track quality and minimal contamination from secondary particles.

Particle-composition correction The measured data are complemented by Monte Carlo simulations implementing a realistic GEANT3 [51] model of the ALICE detector and mimicking the experimental conditions present during the data taking. From these simulations, information about efficiency, secondary contamination, and smearing of N_{ch} as well as p_T is obtained. However, it was found in previous measurements [52, 53] that the current state-of-the-art MC event generators do not perfectly reproduce the relative particle abundances, in particular for hyperons. Since the detector response, as well as the effect of the track selection, vary for the different particle species (e.g. due to different lifetimes), a purely MC-based correction for efficiency and feed-down contamination of inclusive charged particles would depend on the accuracy of the relative hadron abundances produced by the respective underlying event generator. To take this effect into account, the particle abundances from the event generator are re-weighted by means of a data-driven approach that was already employed in other ALICE analyses [8, 42]. This particle-composition correction utilises several ALICE measurements of identified (π, K, p, Λ) particle p_T spectra as a function of multiplicity (in coarse intervals) for a range of collision systems [9, 53–56] as input and offers N_{ch} - and p_T -dependent correction factors for particle abundances. These data-driven adjustments for the generator bias result in a more accurate description of the detector performance and are applied prior to the unfolding corrections described in the following.

Event-level unfolding The measurement of the raw charged-particle multiplicity distribution is influenced by several effects. In the experiment, some collisions that occurred within $|V_z| < 10 \text{ cm}$ with

respect to the nominal interaction vertex are not detected by the minimum-bias trigger or discarded by the subsequent event selection. Due to the experimental vertex-position resolution, a valid collision event may also be reconstructed outside of $|V_z^{\text{meas}}| < 10$ cm and therefore rejected in the analysis. On the other hand, the measured and selected sample of events may contain collisions without any primary charged particle produced within the kinematic range of interest (i.e. events with $N_{\text{ch}} = 0$) or collisions with a true vertex position located outside $|V_z| < 10$ cm. In addition, as discussed before, the value of the measured track multiplicity $N_{\text{ch}}^{\text{meas}}$ itself is affected by tracking efficiency and track selection as well as contamination with secondaries and particles smeared into the kinematic acceptance, resulting in a broad correlation between the actual number of primary charged particles N_{ch} and the measured track multiplicity $N_{\text{ch}}^{\text{meas}}$.

Using the particle-composition corrected MC simulation, the measured track multiplicity distribution can be corrected for the efficiency, contamination, and smearing effects by means of an iterative unfolding procedure proposed by D'Agostini [57] and implemented in the RooUnfold [58] software package.

Starting with an initial assumption (prior) for the desired multiplicity distribution, which in this case is taken from the MC simulation, unfolding weights (posterior probabilities) are calculated by combining the prior with the detector response and the measured track multiplicity distribution according to Bayes' theorem. By again applying these posterior probabilities to the measured track multiplicity distribution, an updated and more accurate guess for the prior is calculated. This procedure is repeated at least three times and, in order to avoid overfitting, immediately stopped once the χ^2/ndf between the resulting multiplicity distributions of two consecutive iterations drops below unity. In this context, the number of degrees of freedom refers to the number of data points in the respective distribution. The procedure is found to be very stable and the resulting unfolded spectrum after convergence is not sensitive to the choice of a prior.

Track-level unfolding While the one-dimensional multiplicity distributions are straightforward to unfold with the iterative D'Agostini method described above, extracting the correlation between p_{T} spectra and the corresponding multiplicity poses a greater challenge. In principle, this two-dimensional (2D) deconvolution could be done in the same manner, i.e., by unfolding the distribution of $(N_{\text{ch}}^{\text{meas}}, p_{\text{T}}^{\text{meas}})$ -pairs and thereby extracting the corrected $(N_{\text{ch}}, p_{\text{T}})$ -distribution of primary charged particles. However, for the highly-granular measurement carried out here, this would imply a huge number of possible combinations and therefore, in practice, require an unreasonably large Monte Carlo event sample to sufficiently populate the smearing matrix that represents the detector response. Hence, in this analysis, a new approach was developed aiming to effectively achieve the 2D unfolding in a simpler way, by splitting it into multiple one-dimensional unfolding problems. Starting from the raw yield of charged-particle tracks as a function of measured track transverse momentum $p_{\text{T}}^{\text{meas}}$ and measured track multiplicity $N_{\text{ch}}^{\text{meas}}$, this technique yields the fully corrected transverse momentum spectra of primary charged particles as a function of their corresponding primary charged particle multiplicity N_{ch} . These fully corrected N_{ch} -dependent p_{T} spectra are then normalised to the number of $N_{\text{ch}} > 0$ events obtained from the unfolded multiplicity distributions. In addition, the spectra are divided by the widths Δp_{T} and ΔN_{ch} of the respective intervals chosen for analysis. In the present work, for pp, p-Pb and AA collisions with $N_{\text{ch}} \leq 100$, multiplicity intervals of $\Delta N_{\text{ch}} = 1$ are used, while for the rest of the range in AA collisions intervals of $\Delta N_{\text{ch}} = 9$ are chosen. This choice is driven by optimising the resolution of the unfolding procedure versus computing time. As the bulk of particles are produced at low transverse momentum, the p_{T} intervals are set to have decreasing granularity from low to high p_{T} .

In the experiment, event-level as well as track-level effects influence whether a charged particle with transverse momentum p_{T} from an event of multiplicity N_{ch} is detected with the measured properties $p_{\text{T}}^{\text{meas}}$ and $N_{\text{ch}}^{\text{meas}}$. For the reasons described above, entire collision events, and in consequence all of their corresponding particles, can either be lost if the event is rejected or incorrectly selected and as a result contribute to the background contained in the measured track sample. Further, for an event which is

selected for analysis, the p_T^{meas} spectrum as well as the measured track multiplicity $N_{\text{ch}}^{\text{meas}}$ are affected by tracking efficiency, transverse momentum resolution, and contamination from secondaries or particles smeared into the kinematic acceptance of the measurement. While the event-level effects change the p_T -integrated detector response and are intrinsically multiplicity dependent, the track-level detector response mainly depends on the transverse momentum of the respective particle. However, there is still a small p_T dependence of contamination and efficiency related to the event selection as the trigger may bias toward specific types of events (e.g., by selectively rejecting diffractive collisions which may have a transverse momentum shape different from that of non-diffractive events with the same multiplicity). On the other hand, also the tracking efficiency and contamination are (slightly) multiplicity dependent, as for instance the particle composition of the event changes with multiplicity, which is relevant in particular for AA collisions.

The basic idea behind the novel procedure employed in this analysis is that the multiplicity dimension (which is mostly affected by event-level effects) and the p_T dimension (which is dominated by track-level effects) can be treated in two separate, sequential unfolding stages. In a first step, the $N_{\text{ch}}^{\text{meas}}$ dependent raw track yield in each p_T^{meas} interval is unfolded separately using the event-level efficiencies and contamination as well as the (p_T integrated) multiplicity smearing matrix of primary charged particles, which contains the probability for a primary charged particle from a collision with true multiplicity N_{ch} to be found in an event with measured track multiplicity $N_{\text{ch}}^{\text{meas}}$. As a result of this deconvolution, the measured tracks are reassigned to the true multiplicities N_{ch} and corrected for track losses related to the event selection and contamination from background events. In a second step, the p_T^{meas} dependent track yield is unfolded individually in each N_{ch} interval using the corresponding p_T dependent tracking efficiencies and p_T^{meas} dependent contamination, as well as the (multiplicity-integrated) transverse momentum smearing matrix of primary charged particles. Note that since the measured track distributions in each of the individually unfolded p_T^{meas} or N_{ch} intervals are different, unique posterior probabilities (i.e., unfolding weights) are obtained in each of these cases. For all of the p_T^{meas} intervals, the p_T^{meas} integrated N_{ch} distribution of measured primary charged particles taken from the MC simulation is used as the initial prior for the unfolding, while for all the N_{ch} intervals the N_{ch} integrated p_T distribution of measured primary charged particles is used.

To validate the self-consistency of this sequential unfolding approach, it is applied to a MC sample which includes the transport of particles through the detector and the results are then compared with its underlying generator-level expectation. In Fig. 2 this closure test is shown for the mean and standard deviation of the unfolded N_{ch} dependent transverse momentum spectra simulated for pp, p–Pb and Pb–Pb collisions at $\sqrt{s_{\text{NN}}} = 5.02$ TeV using the PYTHIA8, EPOS LHC and HIJING [59] event generators, respectively. Note that these are the particle-composition corrected simulations. The ratios in the bottom panels show a very good agreement between the unfolded and generated distributions over the whole range of multiplicities. The non-closure is mostly well below 1% and the remaining relative differences are used as an estimate for the systematic uncertainty of the method. The closure test was validated by cross-checking the largest data set, i.e. pp collisions at $\sqrt{s} = 13$ TeV, with EPOS LHC as an alternative MC generator.

In the top panel of Fig. 3, the evolution of spectral shapes with multiplicity obtained with this unfolding procedure is shown for pp collisions at $\sqrt{s} = 5.02$ TeV. This double-differential measurement not only allows characteristic properties of the spectra, e.g. $\langle p_T \rangle$, and $\sigma(p_T)$, to be extracted but also allows a direct comparison of the spectral shape produced in collisions with different multiplicities. The bottom left panel of Fig. 3 shows the ratio of multiplicity-dependent self normalised p_T distributions $P_{\text{prim}}(p_T|N_{\text{ch}})$ to the multiplicity-integrated self normalised p_T distribution $P_{\text{prim}}(p_T)$ of primary charged particles. A hardening of the spectra with multiplicity is apparent, which continuously increases with N_{ch} , a trend observed earlier in coarser multiplicity intervals [41] and with different event selection methods [60]. In the bottom right panel of Fig. 3 the self normalised multiplicity distribution of primary charged particles

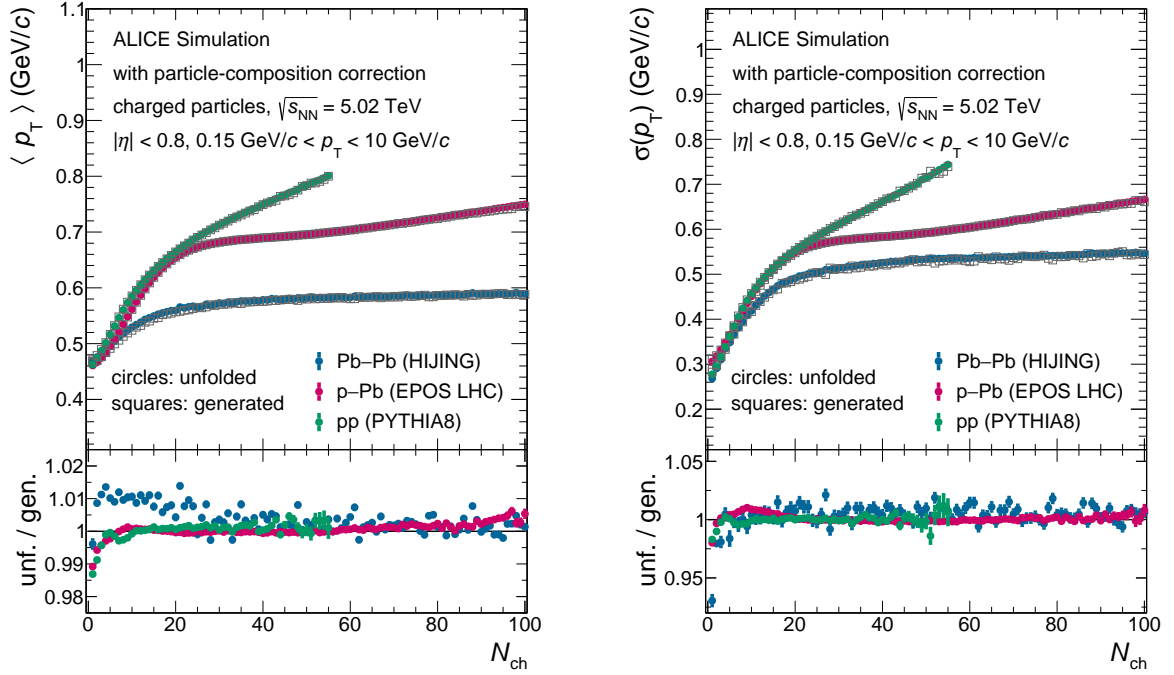


Figure 2: The N_{ch} dependence of the mean (left panel) and standard deviation (right panel) of the p_T distributions for (particle-composition corrected) Monte Carlo events in pp, p–Pb and Pb–Pb collisions at $\sqrt{s_{NN}} = 5.02$ TeV. Results propagated through a full GEANT model of ALICE and corrected with the sequential 2D unfolding (closed circles) procedure described in the text are compared with the generator-level (open squares) distributions and their ratios are shown in the bottom panels.

for fixed transverse momentum $P_{\text{prim}}(N_{\text{ch}}|p_T)$ divided by the p_T -integrated N_{ch} distribution $P_{\text{prim}}(N_{\text{ch}})$ is shown as a function of N_{ch} . As expected, it is evident that high p_T particles are produced mostly in high-multiplicity events.

Systematic uncertainties The accuracy of the corrections applied in this work depends on how well the measured track properties are reproduced by the MC simulations. The systematic uncertainties related to a possible disagreement were estimated by varying the track-selection criteria in reasonable ranges. A detailed list of those track quality criteria and their variations can be found in previous ALICE publications [8, 42]. In order to estimate the systematic uncertainty related to the particle-composition correction, the yields of identified particles are varied within their respective systematic uncertainties and the extrapolation of those spectra to $p_T = 0.15 \text{ GeV}/c$ is performed with different functions. In addition, an uncertainty for the accuracy of the unfolding procedure is assigned that is quantified by the level of agreement between the unfolded simulated measurement and the expected distributions produced by the generator (MC closure test). For each variation, the fully corrected results are calculated and their deviation to the nominal result is considered an uncertainty. Therefore, any effect of the variations on the performance of the analysis procedure is included in the respective systematic uncertainty. To obtain the overall systematic uncertainties, all individual contributions are assumed to be fully uncorrelated and are added in quadrature.

The systematic uncertainties of multiplicity distributions are around 2–5% at low N_{ch} , but increase towards higher multiplicities up to 10–20%, depending on the collision system and energy. While for pp and p–Pb collisions the track quality requirements are the most relevant contributions, in AA collisions the systematic uncertainty related to the particle-composition correction is the most prominent one. The systematic uncertainty of the mean transverse momentum of the unfolded spectra is largely dominated by the contributions from track-selection variations, yet the total systematic uncertainties in most of the

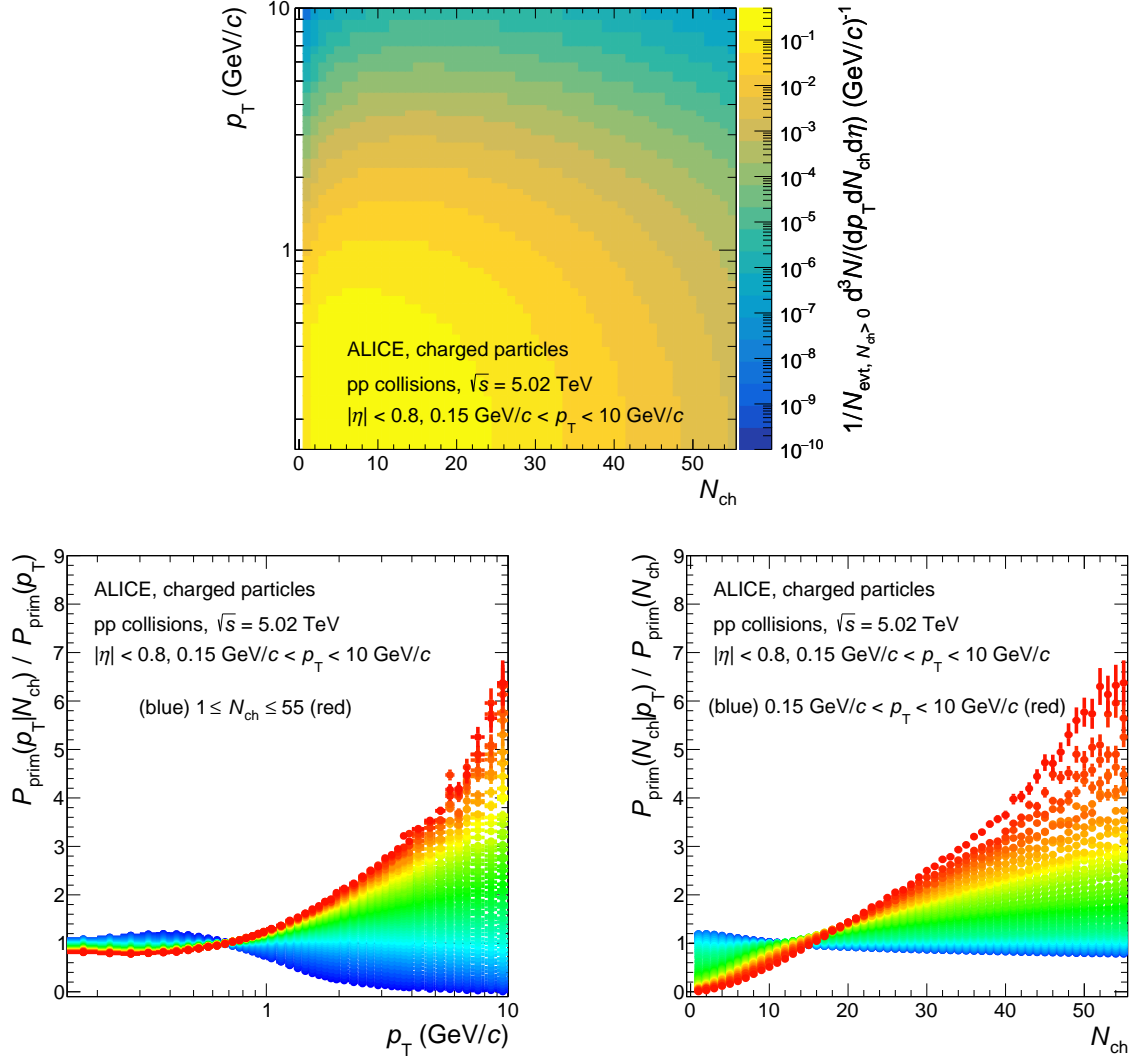


Figure 3: Top panel: the correlation of primary charged particle p_T spectra with multiplicity per $N_{\text{ch}} > 0$ event for pp collisions at $\sqrt{s} = 5.02$ TeV. Bottom panels: the corresponding relative change of p_T (left) and N_{ch} (right) distributions with respect to the inclusive ones. In the left panel, each of the curves represents a single N_{ch} value, ranging from $N_{\text{ch}} = 1$ (blue) to $N_{\text{ch}} = 55$ (red). In the right panel, the colours represent the p_T intervals used in this analysis from the lowest in blue to the highest one in red.

reported N_{ch} range are around 1%. At the lowest and highest multiplicities the contribution from the closure tests increases to up to 2%. The contribution from the particle-composition correction is around 0.5%. The systematic uncertainties of the standard deviation of the spectra $\sigma(p_T)$ are dominated by the track quality requirements and are below 2% on average. At very low and very high N_{ch} , the systematic uncertainties go up to 3–5% due to the MC closure test contribution.

4 Results and discussion

Multiplicity distributions as well as the mean and standard deviation of charged-particle p_T spectra as a function of N_{ch} are presented in comparison with model predictions. Table 2 summarises the mean and standard deviation of both the multiplicity distributions and N_{ch} -integrated p_T spectra for pp, p–Pb, Xe–Xe, and Pb–Pb collisions at the various centre-of-mass energies per nucleon pair.

The left panel of Fig. 4 shows the probability density of charged-particle multiplicity N_{ch} for pp (top),

Table 2: Global characteristics of the analysed data sets with corresponding systematic uncertainties. Both the N_{ch} and the p_{T} spectra are consistently defined in the kinematic range $|\eta| < 0.8$ and $0.15 \text{ GeV}/c < p_{\text{T}} < 10 \text{ GeV}/c$ and only events with $N_{\text{ch}} > 0$ are considered.

	$\sqrt{s_{\text{NN}}} \text{ (TeV)}$	$\langle N_{\text{ch}} \rangle$	$\sigma(N_{\text{ch}})$	$\langle p_{\text{T}} \rangle_{\text{incl}} \text{ (MeV}/c)$	$\sigma(p_{\text{T}})_{\text{incl}} \text{ (MeV}/c)$
pp	2.76	7.18 ± 0.24	6.05 ± 0.17	589.7 ± 2.6	483 ± 4
	5.02	8.21 ± 0.10	7.20 ± 0.08	612.2 ± 2.7	520.2 ± 1.0
	7	8.86 ± 0.12	7.88 ± 0.11	627.1 ± 1.6	541.3 ± 2.1
	8	9.05 ± 0.22	8.11 ± 0.18	631 ± 5	547 ± 4
	13	10.31 ± 0.09	9.48 ± 0.07	654.0 ± 1.0	582.4 ± 0.9
p–Pb	5.02	25.51 ± 0.25	19.79 ± 0.20	711.9 ± 1.3	619.8 ± 1.1
	8.16	29.56 ± 0.26	23.13 ± 0.23	741.5 ± 1.4	657.0 ± 1.3
Xe–Xe	5.44	458 ± 10	514 ± 13	717.4 ± 1.8	568.4 ± 1.4
Pb–Pb	2.76	573 ± 9	667 ± 12	687.3 ± 1.3	528.0 ± 1.7
	5.02	682 ± 13	819 ± 16	724.1 ± 1.1	564.9 ± 1.0

p–Pb (middle), and AA (bottom) collisions at different energies per nucleon pair. For all collision systems, the distributions reach a maximum around $N_{\text{ch}} \approx 2$ and then fall steeply off over several orders of magnitude. In the pp and p–Pb systems, the slope of the decay with N_{ch} decreases with increasing collision energy. This can be attributed to the larger momentum transfer in the initial hard scattering which results in larger multiplicities. The right panel of Fig. 4 presents the data after scaling the probability density and the charged-particle multiplicity with the average number of charged particles $\langle N_{\text{ch}} \rangle$ according to the Koba–Nielsen–Olesen (KNO) [61] scaling. Figure 5 shows the corresponding ratios of the KNO-scaled multiplicity distributions at various centre-of-mass energies per nucleon pair relative to $\sqrt{s} = 13 \text{ TeV}$, $\sqrt{s_{\text{NN}}} = 8.16 \text{ TeV}$ and $\sqrt{s_{\text{NN}}} = 5.02 \text{ TeV}$ for pp, p–Pb and Pb–Pb collisions, respectively. KNO scaling apparently holds in pp and AA collisions within 20%, and in p–Pb collisions within 10%.

In Fig. 6 the mean and standard deviation of the p_{T} spectra are compared for pp, p–Pb and Pb–Pb collisions at the same centre-of-mass energy per nucleon pair of $\sqrt{s_{\text{NN}}} = 5.02 \text{ TeV}$. All three collision systems have similar values at $N_{\text{ch}} = 1$ and then coincide until Pb–Pb deviates at $N_{\text{ch}} \approx 5$ and p–Pb deviates at $N_{\text{ch}} \approx 25$ from the trend observed in pp. This observation is consistent with an earlier comparison of the $\langle p_{\text{T}} \rangle$ – N_{ch} correlation for the three systems at different centre-of-mass energies [62]. Figure 7 shows the mean (left) and standard deviation (right) of the transverse momentum spectra as a function of the charged-particle multiplicity N_{ch} for pp (top), p–Pb (middle), and AA (bottom) collisions at different centre-of-mass energies per nucleon pair. For all collision systems, a clear ordering of $\langle p_{\text{T}} \rangle$ as well as $\sigma(p_{\text{T}})$ with collision energy is observed, which can be attributed to the larger momentum transfers involved at higher $\sqrt{s_{\text{NN}}}$. For pp collisions at all centre-of-mass energies, the average transverse momentum increases monotonically with an almost linear trend up to $N_{\text{ch}} \approx 16$ and beyond that continues with an again almost linear dependence on N_{ch} but reduced slope. In p–Pb collisions, a similar multiplicity dependence is observed up to $N_{\text{ch}} \approx 25$. At higher multiplicities, the increase in $\langle p_{\text{T}} \rangle$ is slower than in pp collisions. In both pp and p–Pb, $\sigma(p_{\text{T}})$ follows a similar trend as $\langle p_{\text{T}} \rangle$. On the other hand, for AA collisions one observes an increase of $\langle p_{\text{T}} \rangle$ with multiplicity up to about one third of the measured range, followed by a constant trend for the rest of the N_{ch} range. The $\sigma(p_{\text{T}})$ increases for $N_{\text{ch}} \lesssim 100$ to a maximum and decreases afterwards. This is unique to large collision systems and is presumably a consequence of flow and jet quenching [8]. The high N_{ch} resolution of this measurement makes it possible to spot differences between the spectral evolution with multiplicity in Xe–Xe and Pb–Pb collisions at $\sqrt{s_{\text{NN}}} = 5.44 \text{ TeV}$ and $\sqrt{s_{\text{NN}}} = 5.02 \text{ TeV}$, respectively. The observed difference in the trends might be a result of the slightly deformed Xe nuclei [63]. In Fig. 8 both the mean (left) and standard deviation (right) of the p_{T} spectra as a function of N_{ch} are summarised for all data sets (top panels) and then shown as a function of relative multiplicity $N_{\text{ch}}/\langle N_{\text{ch}} \rangle$ (middle panels) as well as divided by their respective multiplicity-integrated values (bottom panels). In the latter scaling, the overall energy-dependent

increase of average kinematic energy and number of produced particles are accounted for. As a result, the values for each collision system align almost perfectly for $\langle p_T \rangle / \langle p_T \rangle_{\text{incl}}$ and $\sigma(p_T) / \sigma(p_T)_{\text{incl}}$.

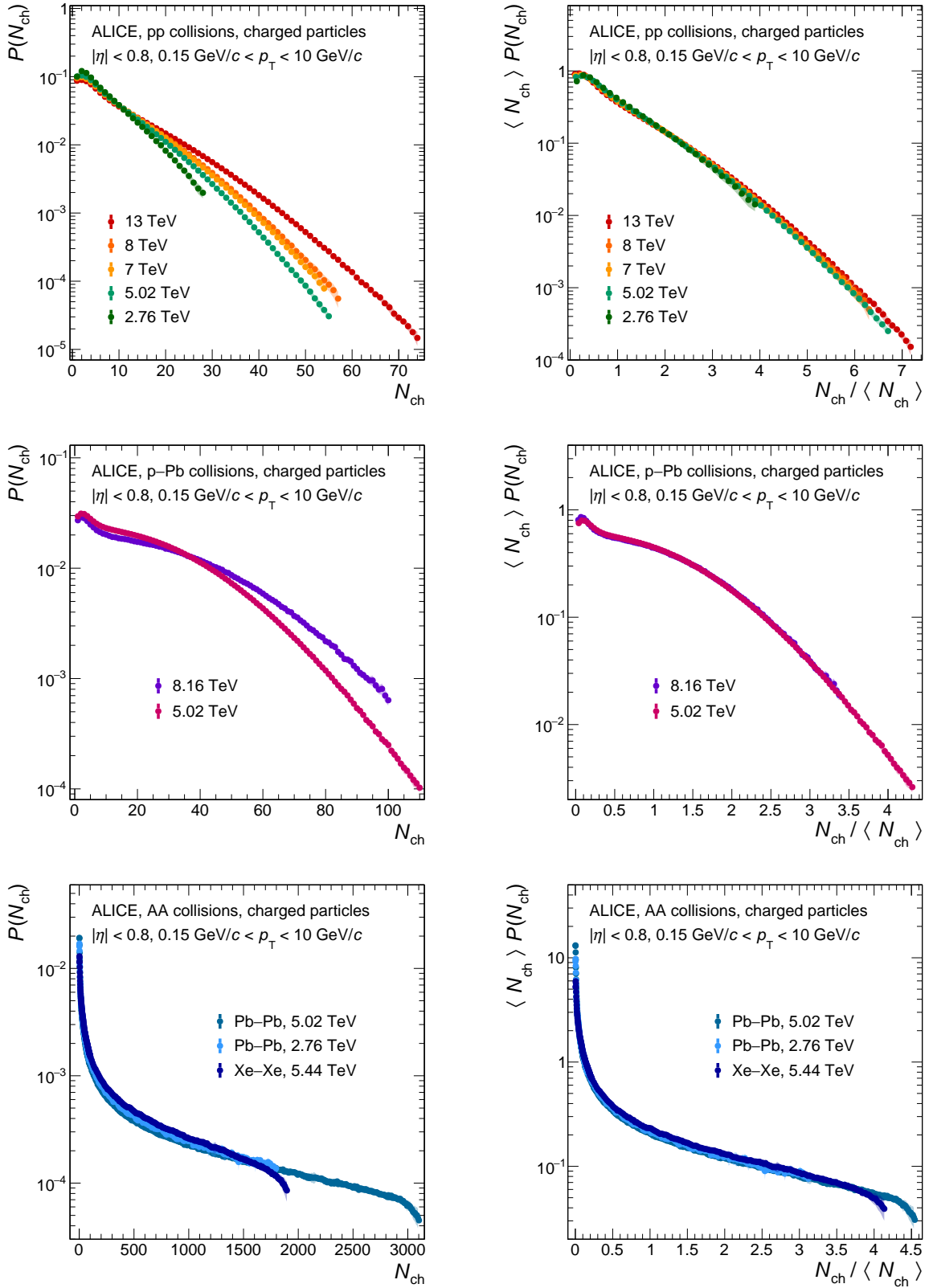


Figure 4: Probability density of charged-particle multiplicity N_{ch} (left) and the corresponding KNO-scaled distributions (right) for pp (top), p-Pb (middle), and AA (bottom) collisions at different centre-of-mass energies per nucleon pair. Statistical and systematic uncertainties are shown as bars and semi-transparent bands, respectively.

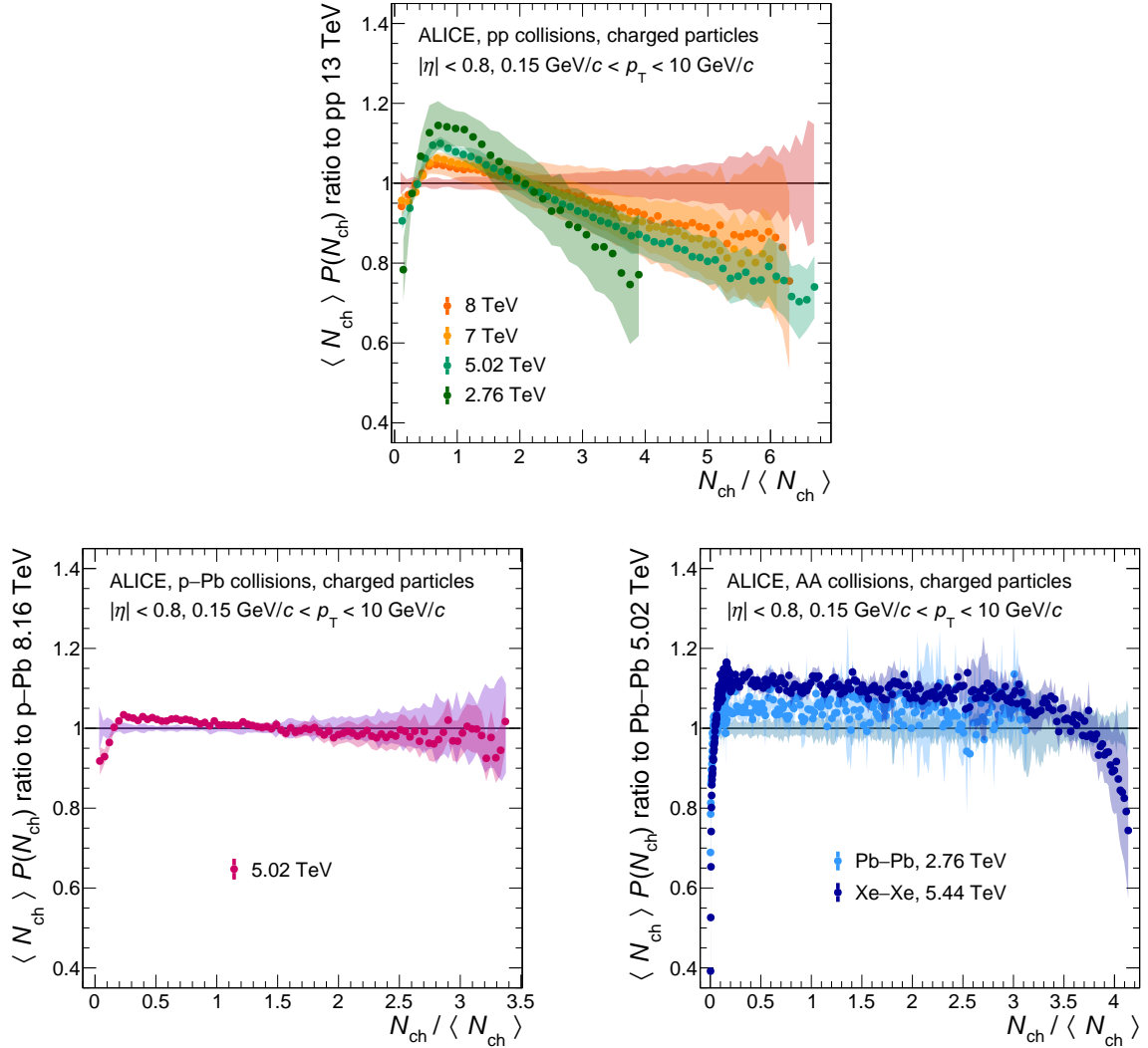


Figure 5: Ratios of the KNO-scaled multiplicity distributions at various centre-of-mass energies per nucleon pair relative to $\sqrt{s} = 13$ TeV for pp collisions (top panel) and relative to $\sqrt{s_{\text{NN}}} = 8.16$ TeV and $\sqrt{s_{\text{NN}}} = 5.02$ TeV for p-Pb and Pb-Pb collisions, respectively (left and right bottom panels). Statistical and systematic uncertainties are shown as bars and semi-transparent bands, respectively.

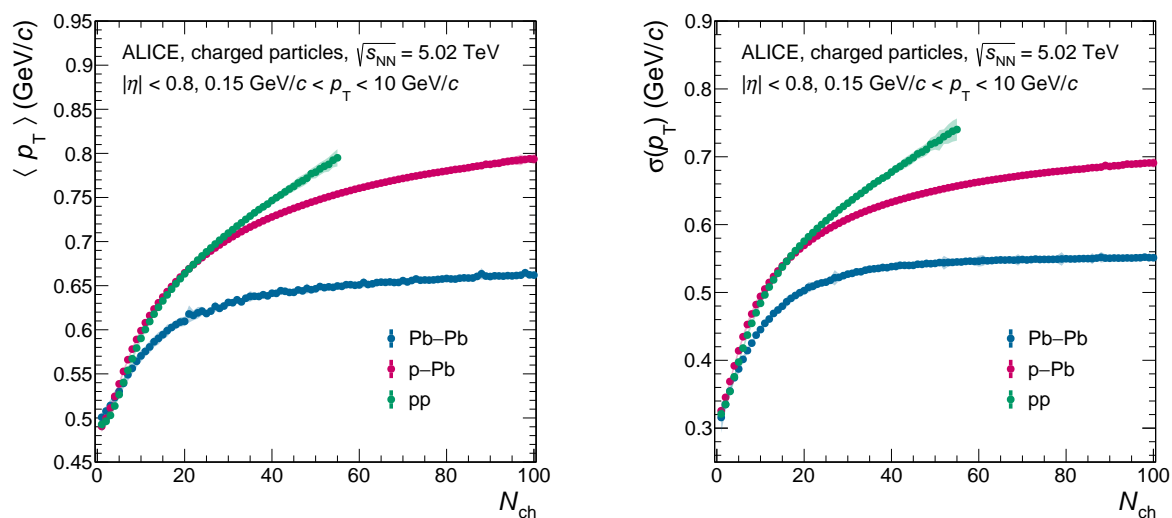


Figure 6: Mean (left) and standard deviation (right) of the charged-particle transverse momentum spectra as a function of the charged-particle multiplicity for pp, p-Pb, and Pb-Pb collisions at a centre-of-mass energy per nucleon pair of $\sqrt{s_{NN}} = 5.02$ TeV. Statistical and systematic uncertainties are shown as bars and semi-transparent bands, respectively.

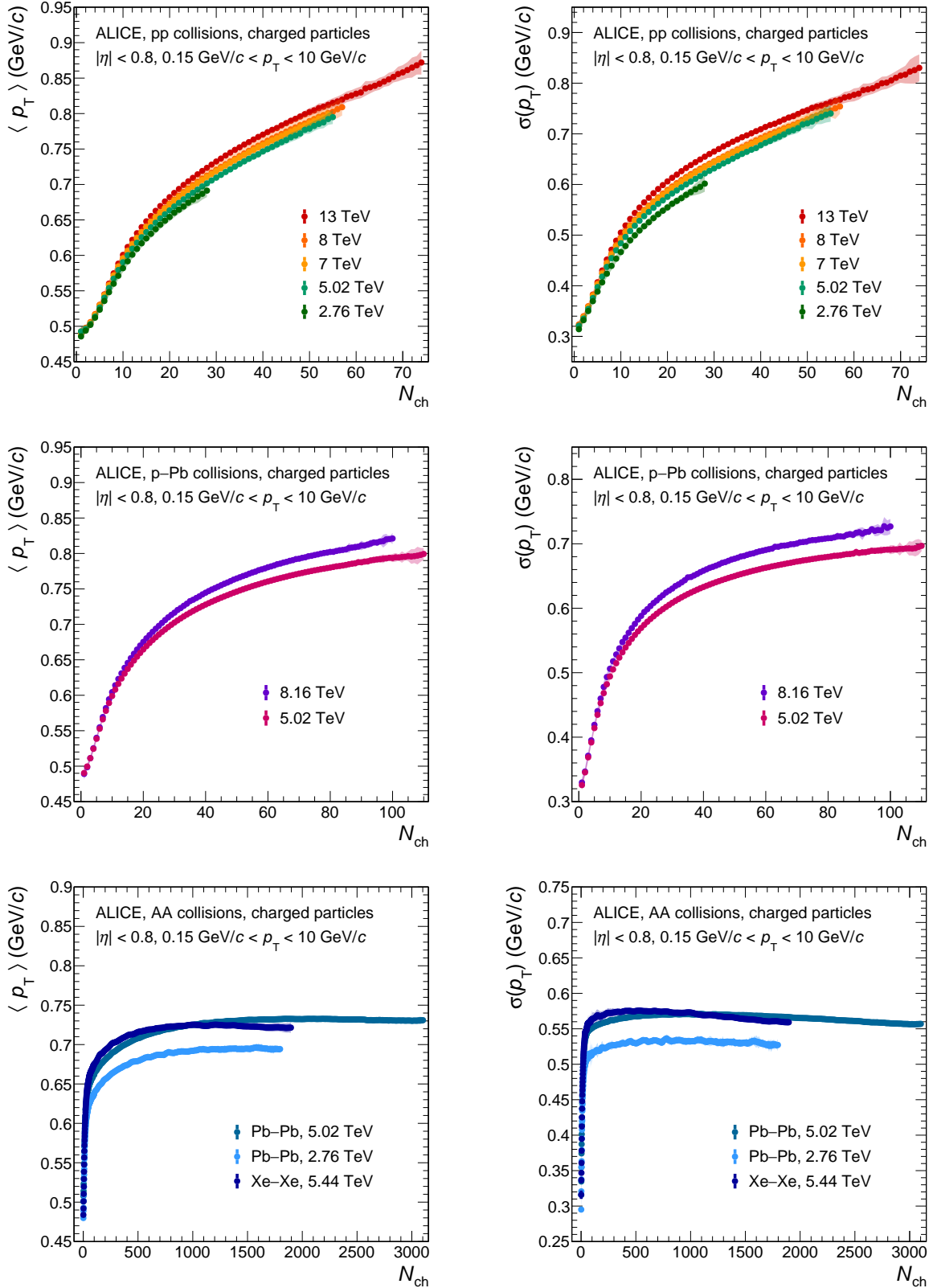


Figure 7: Mean (left) and standard deviation (right) of the charged-particle transverse momentum spectra as a function of the charged-particle multiplicity for pp (top), p-Pb (middle), and AA (bottom) collisions at different centre-of-mass energies per nucleon pair. Statistical and systematic uncertainties are shown as bars and semi-transparent bands, respectively.

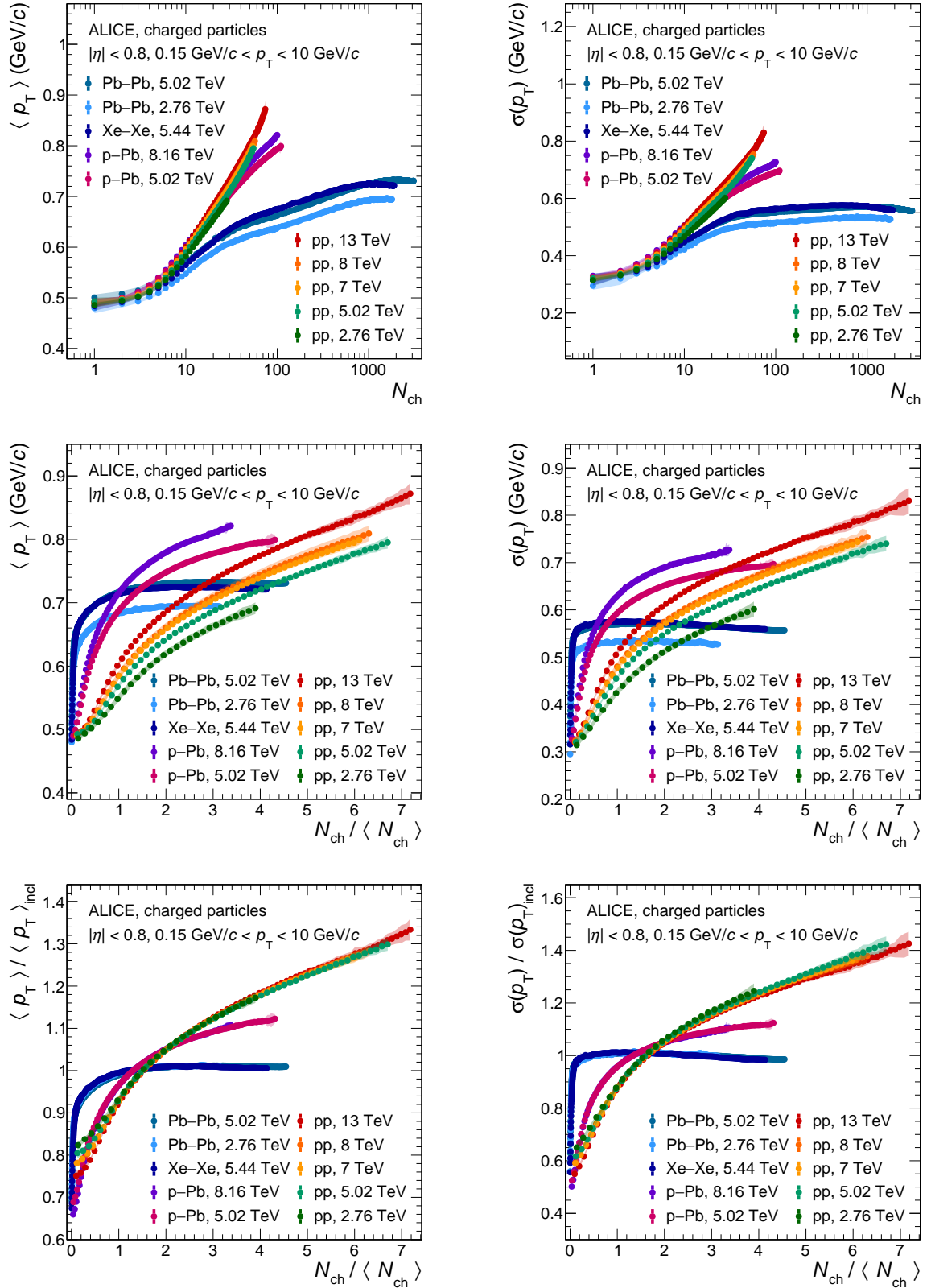


Figure 8: Mean (left) and standard deviation (right) of the charged-particle transverse momentum spectra as a function of the charged-particle multiplicity (top) and relative multiplicity $N_{ch}/\langle N_{ch} \rangle$ (middle, bottom) for pp, p-Pb, Xe-Xe and Pb-Pb collisions at various centre-of-mass energies per nucleon pair. The bottom panels show both quantities relative to their multiplicity-inclusive value. Statistical and systematic uncertainties are shown as bars and semi-transparent bands, respectively.

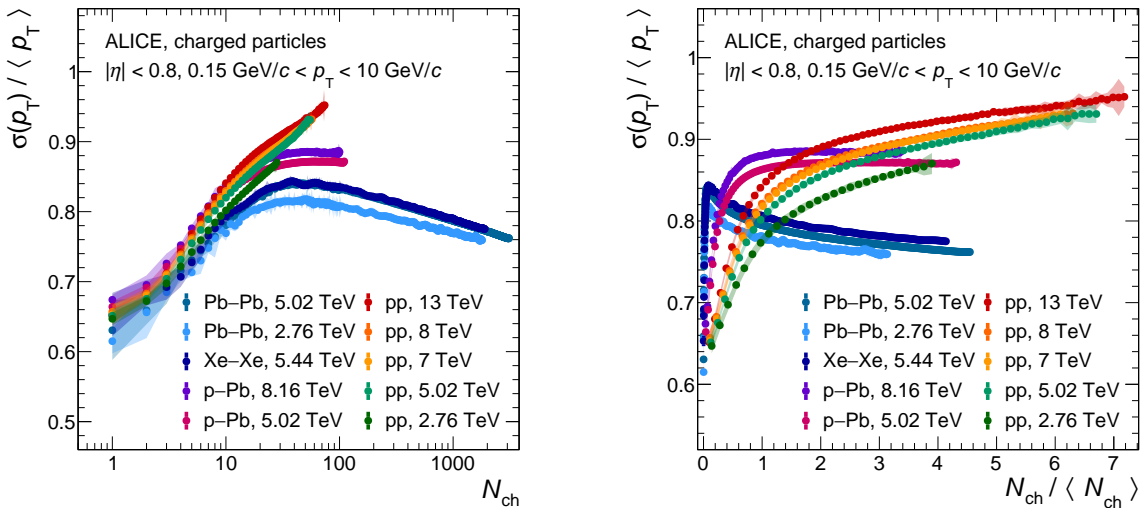


Figure 9: Relative standard deviation of the charged-particle transverse momentum spectra as a function of the absolute (left) and relative (right) charged-particle multiplicity for pp, p–Pb, Xe–Xe and Pb–Pb collisions at various centre-of-mass energies per nucleon pair. Statistical and systematic uncertainties are shown as bars and semi-transparent bands, respectively.

The left panel of Fig. 9 shows the relative standard deviation of the spectra $\sigma(p_T)/\langle p_T \rangle$ as a function of N_{ch} (left) and as a function of $N_{ch}/\langle N_{ch} \rangle$ (right). For pp collisions, this relative width of the p_T spectra increases with multiplicity. The same trend is also observed for the larger collision systems. However, after around $N_{ch} \approx 20$ both for p–Pb and AA collisions, the standard deviation rises at the same rate as the mean, resulting in a flattening of the $\sigma(p_T)/\langle p_T \rangle$ ratio. After this plateau, the spectra in AA collisions become narrower relative to their mean values. The right panel of Fig. 9 shows the relative standard deviation of the spectra $\sigma(p_T)/\langle p_T \rangle$ as a function of the relative multiplicity $N_{ch}/\langle N_{ch} \rangle$. The plateau observed in p–Pb collisions starts at the relative multiplicity $N_{ch}/\langle N_{ch} \rangle \approx 1$, while the decrease observed in AA collision already begins at lower relative multiplicities of around $N_{ch}/\langle N_{ch} \rangle \approx 0.2$.

Figures 10 and 11 compare measured results for pp and p–Pb collisions with predictions from PYTHIA8 (solid lines) and EPOS LHC (dashed lines). Here, the PYTHIA8.306 event generator is used with the Monash-2013 tune [31] for pp collisions and with the Angantyr model [26] for p–Pb collisions. The top left panel represents the ratio of models over measurements for the multiplicity distributions, the top right panel for the respective KNO-scaled multiplicity distributions and the bottom left and right panel show the ratios for $\langle p_T \rangle$ and $\sigma(p_T)$, respectively.

In pp collisions, the overall shapes of the multiplicity distribution and KNO-scaled distribution shown in the upper panels of Fig. 10 are better described by EPOS LHC, while PYTHIA8 falls sharply off above $N_{ch}/\langle N_{ch} \rangle \approx 4$. Both models agree with the experimental distributions within 25% with larger deviations at highest multiplicities. For $\langle p_T \rangle$ and $\sigma(p_T)$ shown in the bottom panels of Fig. 10, PYTHIA8 underpredicts the experimental data on $\langle p_T \rangle$ at the lowest values of N_{ch} by up to 4%. The N_{ch} dependent $\langle p_T \rangle$ values produced by PYTHIA8 increase faster than the measurements with an almost linear dependence up to $N_{ch} \approx 20$, after which the ratio shows a flat multiplicity dependence with an offset from unity varying from 0.5% at $\sqrt{s} = 5.02 \text{ TeV}$ up to 4% at the highest centre-of-mass energy. EPOS LHC is further off at low multiplicities by up to 5% and increases slower than the measurements, underestimating them by up to 6% around $N_{ch} \approx 9$. At higher multiplicities, the increase is faster with a linearly rising ratio up to $N_{ch} \approx 20 - 30$, reaching a plateau which describes the measurements within $\pm 2\%$. The experimental data on $\sigma(p_T)$ is reproduced by both models within 10% at charged-particle multiplicities $N_{ch} > 10$, with larger deviations at the lowest multiplicities.

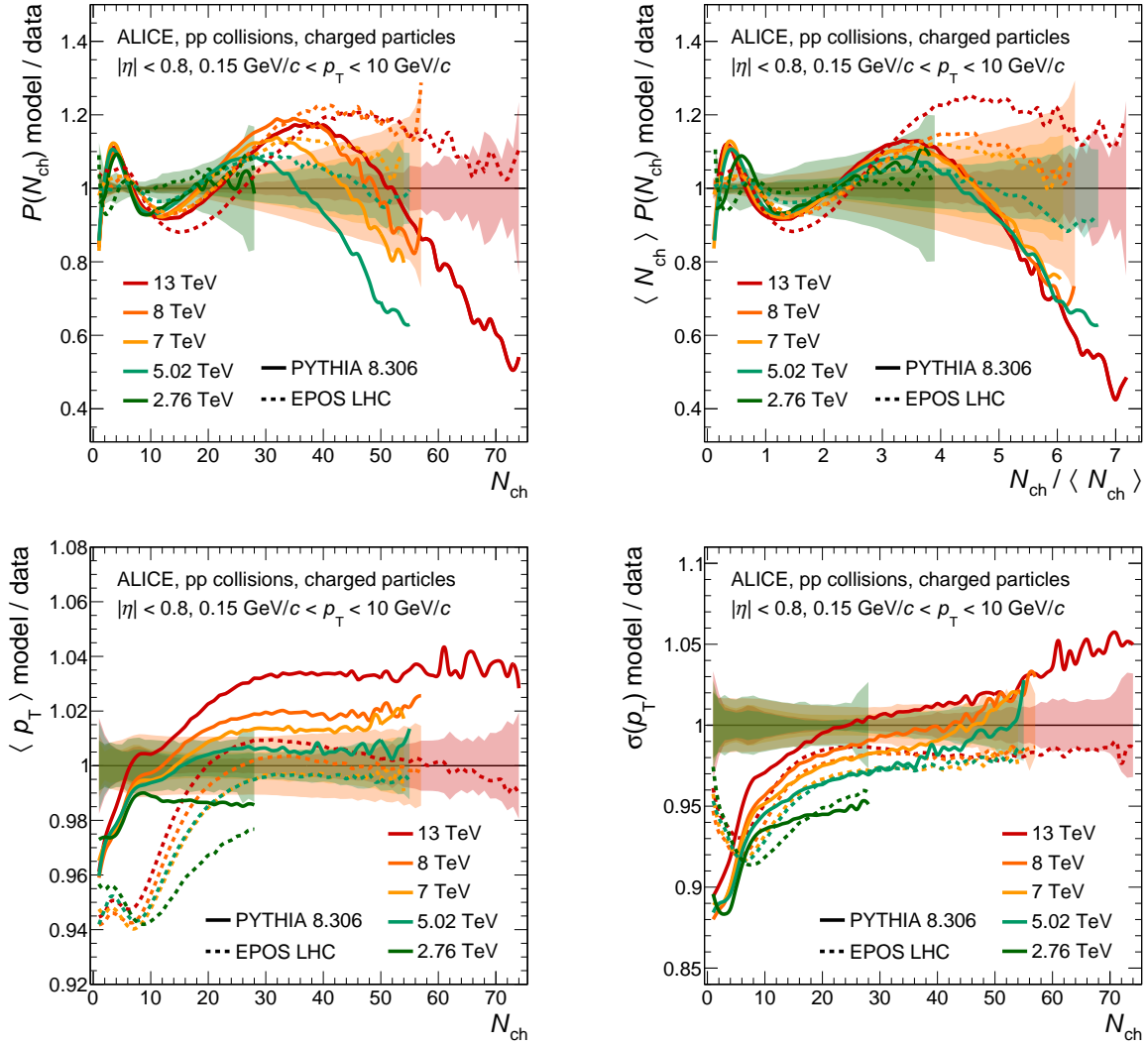


Figure 10: Ratio of model predictions to data for pp collisions at various energies. The upper panels show it for the multiplicity distributions (left) and their KNO-scaling form (right), the bottom panels represent $\langle p_T \rangle$ (left) and $\sigma(p_T)$ (right). The semi-transparent bands indicate the relative systematic uncertainties of the data.

Results from model calculations in comparison with measurements from p–Pb collisions are shown in Fig. 11. PYTHIA8/Angantyr predicts the charged-particle multiplicity distribution within 30% (Fig. 11, top left) over the whole multiplicity range. EPOS LHC agrees within 20% for $N_{\text{ch}} < 70$ but fails to describe the measurement at higher multiplicities. The KNO-scaled multiplicity distributions shown in the top right panel of Fig. 11 are described by both models within 20% up to a relative multiplicity of 2.5. Beyond that, both models exhibit increasing deviations from the measurement. PYTHIA8/Angantyr underpredicts $\langle p_T \rangle$ by about 5% at low multiplicities (Fig. 11, bottom left), $N_{\text{ch}} < 20$, with the deviation increasing as a function of multiplicity, reaching about 25% at $N_{\text{ch}} = 110$. This might result from the missing colour reconnection between the sub-collisions in the model. It is expected that high string density effects, as the recently-introduced showing mechanism [64], will lead to an increase of $\langle p_T \rangle$ as a function of the multiplicity. EPOS LHC reproduces the $\langle p_T \rangle$ and $\sigma(p_T)$ measurement within 10%.

Figure 12 shows a comparison of the measured $\langle p_T \rangle$ as a function of N_{ch} for pp, p–Pb and Pb–Pb collisions at the same centre-of-mass energy per nucleon pair, $\sqrt{s_{\text{NN}}} = 5.02$ TeV, with results from three different model calculations: PYTHIA8 (left panel; Angantyr for p–Pb and Pb–Pb), EPOS3 (middle panel), and hydrodynamics with CGC initial conditions [20] (right panel). As shown before, PYTHIA8

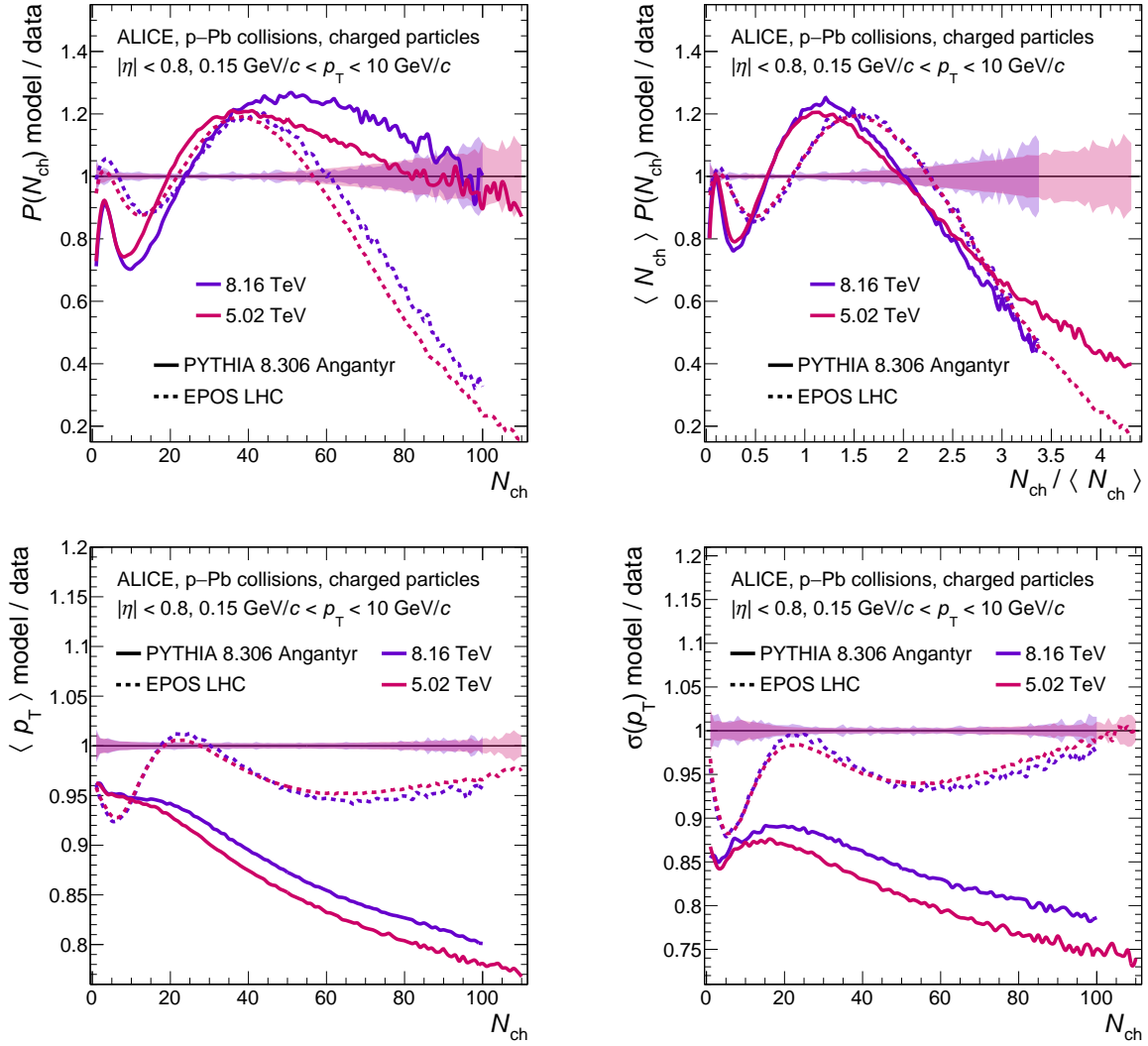


Figure 11: Ratio of model predictions to data for p–Pb collisions at various energies. The upper panels show it for the multiplicity distributions (left) and their KNO-scaling form (right), the bottom panels represent $\langle p_{\text{T}} \rangle$ (left) and $\sigma(p_{\text{T}})$ (right). The semi-transparent bands indicate the relative systematic uncertainties of the data.

describes the pp measurements very well over the entire multiplicity range, even at the highest multiplicities. However, it significantly underpredicts the p–Pb measurements above $N_{\text{ch}} > 10$, where the deviation increases with multiplicity. In Pb–Pb collisions, the $\langle p_{\text{T}} \rangle$ is systematically underpredicted by PYTHIA8/Angantyr by around 8% on average. Again, this points to the missing treatment of high string density effects which are not included in the PYTHIA8/Angantyr model, yet [26]. The EPOS3 model overpredicts the $\langle p_{\text{T}} \rangle$ in all systems up to $N_{\text{ch}} \approx 10 - 20$, and underpredicts p–Pb and Pb–Pb measurements at higher multiplicities, less than PYTHIA8/Angantyr, but also cannot reproduce the $\langle p_{\text{T}} \rangle$ evolution with N_{ch} . The hydrodynamical model calculations do not describe the measurements well, except for Pb–Pb collisions at the highest multiplicities of $N_{\text{ch}} > 1000$.

In the CGC approach, the average transverse momentum is a universal function of the ratio of charged-particle multiplicity and transverse area of a collision [44]. The transverse area $S_{\text{T}}(N_{\text{ch}})$ is derived from the interaction radius $R(\sqrt[3]{dN_{\text{g}}/dy})$ as a function of gluon multiplicity dN_{g}/dy . This interaction radius was calculated within the CGC framework for pp collisions at a reference energy of $\sqrt{s} = 7 \text{ TeV} = W_{0,\text{pp}}$ and for p–Pb collisions at $\sqrt{s_{\text{NN}}} = 5.02 \text{ TeV} = W_{0,\text{p-Pb}}$ [65]. Parameterisations of these interaction radii proposed in Ref. [22] are used to calculate the interaction area. Following the arguments in Ref. [44],

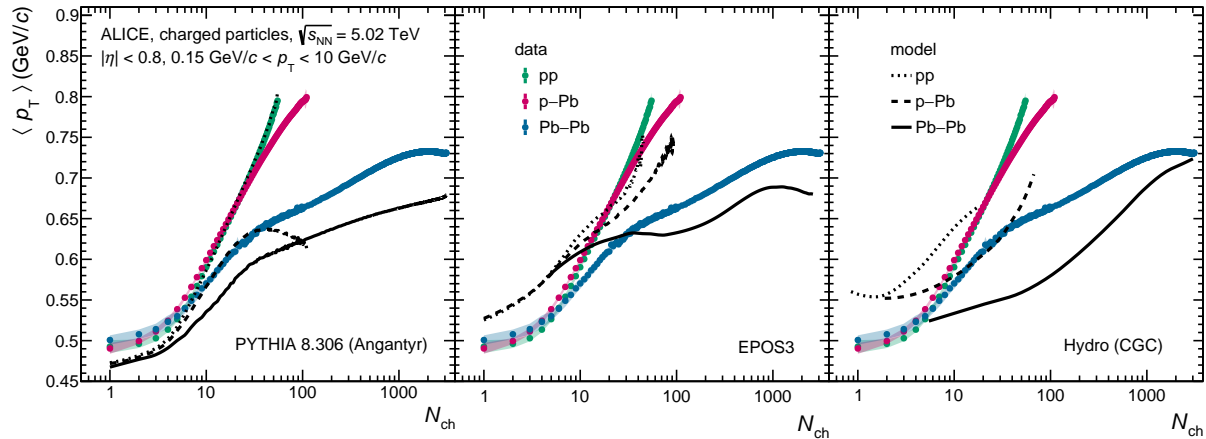


Figure 12: Comparisons of $\langle p_T \rangle$ as a function of N_{ch} at $\sqrt{s_{NN}} = 5.02$ TeV for pp, p–Pb, and Pb–Pb collisions to three different model predictions. Statistical and systematic uncertainties are shown as bars and semi-transparent bands, respectively.

the $\langle p_T \rangle$ vs. N_{ch} measurements presented in this Letter are scaled for each collision energy $W = \sqrt{s_{NN}}$ for the respective collision system (pp, p–Pb) with a factor of $(W/W_0)^{\lambda/(\lambda+2)}$. Here, the exponent λ characterises the saturation scale and was determined in Ref. [44] to be $\lambda = 0.22$ as the best fit to the transverse momentum distributions measured with ALICE. In order to approximate the gluon density corresponding to a measured final state multiplicity, a proportionality factor γ , defined by the equation $dN_g/dy = \gamma N_{ch}$, is needed. Here, the naive value $\gamma = 3/2 \frac{1}{\Delta\eta}$ motivated by the ratio of the number of charged particles to all particles, as done in Ref. [22], is used. A weak dependence of the results on γ was observed. Figure 13 shows the $\langle p_T \rangle$ as a function of $(W/W_0)^{\lambda/(\lambda+2)} \sqrt{N_{ch}/S_T}$ for pp and p–Pb collisions at various collision energies (left), and the ratio of those curves to the 13 TeV result (right), which has the highest reach in this scaling observable. The disagreement from the scaling is significant given the measurement’s uncertainties, but still within about 10% over the entire range. At comparable values of the scaling variable, the ratio shows a distinct energy ordering, and all ratios exhibit a noticeable peak. In a more recent study [66], the determination of the exponent λ was revisited and it was found that the differential cross sections are better described when using $\lambda \approx 0.32$ instead of $\lambda = 0.22$. However, with this updated value for the characteristic exponent λ , the geometrical scaling of the data presented in this Letter agrees only within $\pm 15\%$. In general, the scaling results are found to be very sensitive to the value of λ and the best agreement is actually found for $\lambda = 0$, which effectively removes the energy scaling term $(W/W_0)^{\lambda/(\lambda+2)}$ proposed in Ref. [44]. An approximate geometrical scaling of $\langle p_T \rangle$ was also observed in AA collisions as discussed in Ref. [67].

5 Summary and conclusions

A comprehensive study of inclusive charged-particle production at the LHC is presented, spanning a wide range of collision energies in pp, p–Pb, Xe–Xe and Pb–Pb collisions. Multiplicity distributions are compared across centre-of-mass energies for all collision systems, and, in addition, shown in the KNO-scaling form. The KNO scaling is observed to hold within about 20%, not only for pp collisions, but also for p–Pb and AA collisions. Transverse momentum spectra are measured as a function of charged-particle multiplicity in narrow N_{ch} intervals. The mean and standard deviation of these p_T spectra as a function of N_{ch} are compared with PYTHIA8 (Angantyr), EPOS LHC, EPOS3, and hydrodynamical model predictions. For pp collisions, the spectral shape evolution with multiplicity is described fairly well by PYTHIA8 and EPOS LHC for all centre-of-mass energies, while EPOS3 and the hydrodynamical model fail to predict this observable. In general, for p–Pb and AA collisions there is a large tension with the data for all considered models, except for EPOS LHC which offers the best model prediction for

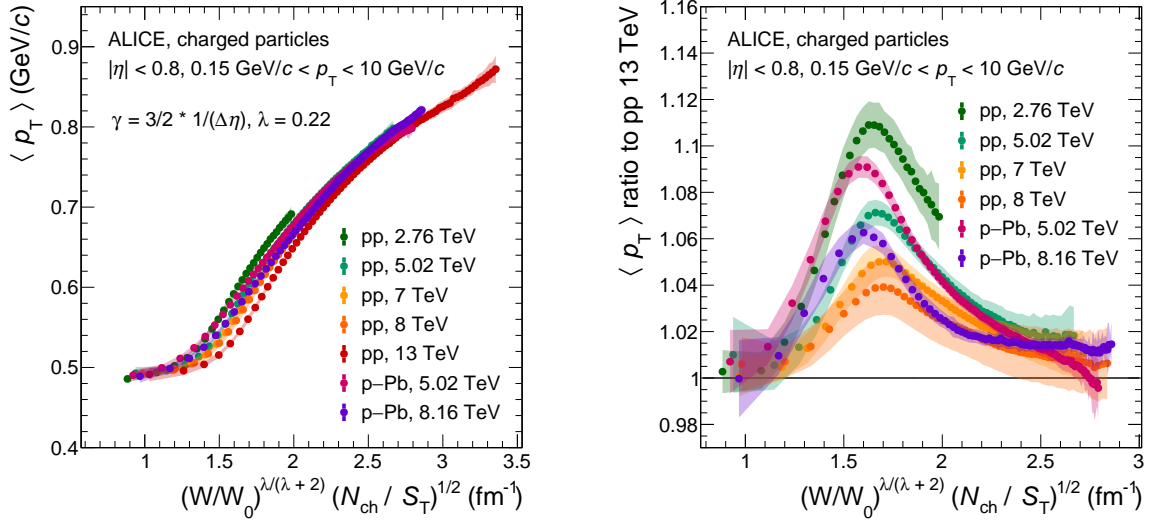


Figure 13: Average transverse momentum $\langle p_T \rangle$ as a function of the scaling variable $(W/W_0)^{\lambda/(\lambda+2)} \sqrt{N_{ch}/S_T}$ [44] for pp and p–Pb collisions at various energies (left) and the ratio of all data sets to that in pp collisions at 13 TeV (right). The reference energy W_0 corresponds to $\sqrt{s} = 7$ TeV for pp and $\sqrt{s_{NN}} = 5.02$ TeV for p–Pb collisions. Statistical and systematic uncertainties are shown as bars and semi-transparent bands, respectively.

p–Pb collisions. The geometric scaling of $\langle p_T \rangle$ proposed within the colour glass condensate framework is found to hold in first order, with deviations at the level of 10%.

Since the study of charged-particle production as a function of multiplicity plays a key role in understanding the properties of strongly-interacting matter created in collision systems of different sizes and energy densities, in the future, this rich high-precision set of multidimensional measurements can help to improve the theoretical modelling of the complex interplay of hard and soft QCD processes that govern particle production at LHC energies.

Acknowledgements

We thank Klaus Werner for providing the EPOS3 predictions and Björn Schenke, Prithwish Tribedy and Chun Shen for the hydrodynamical calculations. We are grateful to Larry McLerran and Michal Praszalowicz for discussions on the geometrical scaling.

The ALICE Collaboration would like to thank all its engineers and technicians for their invaluable contributions to the construction of the experiment and the CERN accelerator teams for the outstanding performance of the LHC complex. The ALICE Collaboration gratefully acknowledges the resources and support provided by all Grid centres and the Worldwide LHC Computing Grid (WLCG) collaboration. The ALICE Collaboration acknowledges the following funding agencies for their support in building and running the ALICE detector: A. I. Alikhanyan National Science Laboratory (Yerevan Physics Institute) Foundation (ANSL), State Committee of Science and World Federation of Scientists (WFS), Armenia; Austrian Academy of Sciences, Austrian Science Fund (FWF): [M 2467-N36] and Nationalstiftung für Forschung, Technologie und Entwicklung, Austria; Ministry of Communications and High Technologies, National Nuclear Research Center, Azerbaijan; Conselho Nacional de Desenvolvimento Científico e Tecnológico (CNPq), Financiadora de Estudos e Projetos (Finep), Fundação de Amparo à Pesquisa do Estado de São Paulo (FAPESP) and Universidade Federal do Rio Grande do Sul (UFRGS), Brazil; Bulgarian Ministry of Education and Science, within the National Roadmap for Research Infrastructures 2020–2027 (object CERN), Bulgaria; Ministry of Education of China (MOEC), Ministry of Science & Technology of China (MSTC) and National Natural Science Foundation of China (NSFC),

China; Ministry of Science and Education and Croatian Science Foundation, Croatia; Centro de Aplicaciones Tecnológicas y Desarrollo Nuclear (CEADEN), Cubaenergía, Cuba; Ministry of Education, Youth and Sports of the Czech Republic, Czech Republic; The Danish Council for Independent Research — Natural Sciences, the VILLUM FONDEN and Danish National Research Foundation (DNRF), Denmark; Helsinki Institute of Physics (HIP), Finland; Commissariat à l’Energie Atomique (CEA) and Institut National de Physique Nucléaire et de Physique des Particules (IN2P3) and Centre National de la Recherche Scientifique (CNRS), France; Bundesministerium für Bildung und Forschung (BMBF) and GSI Helmholtzzentrum für Schwerionenforschung GmbH, Germany; General Secretariat for Research and Technology, Ministry of Education, Research and Religions, Greece; National Research, Development and Innovation Office, Hungary; Department of Atomic Energy Government of India (DAE), Department of Science and Technology, Government of India (DST), University Grants Commission, Government of India (UGC) and Council of Scientific and Industrial Research (CSIR), India; National Research and Innovation Agency - BRIN, Indonesia; Istituto Nazionale di Fisica Nucleare (INFN), Italy; Japanese Ministry of Education, Culture, Sports, Science and Technology (MEXT) and Japan Society for the Promotion of Science (JSPS) KAKENHI, Japan; Consejo Nacional de Ciencia (CONACYT) y Tecnología, through Fondo de Cooperación Internacional en Ciencia y Tecnología (FONCICYT) and Dirección General de Asuntos del Personal Académico (DGAPA), Mexico; Nederlandse Organisatie voor Wetenschappelijk Onderzoek (NWO), Netherlands; The Research Council of Norway, Norway; Commission on Science and Technology for Sustainable Development in the South (COMSATS), Pakistan; Pontificia Universidad Católica del Perú, Peru; Ministry of Education and Science, National Science Centre and WUT ID-UB, Poland; Korea Institute of Science and Technology Information and National Research Foundation of Korea (NRF), Republic of Korea; Ministry of Education and Scientific Research, Institute of Atomic Physics, Ministry of Research and Innovation and Institute of Atomic Physics and University Politehnica of Bucharest, Romania; Ministry of Education, Science, Research and Sport of the Slovak Republic, Slovakia; National Research Foundation of South Africa, South Africa; Swedish Research Council (VR) and Knut & Alice Wallenberg Foundation (KAW), Sweden; European Organization for Nuclear Research, Switzerland; Suranaree University of Technology (SUT), National Science and Technology Development Agency (NSTDA), Thailand Science Research and Innovation (TSRI) and National Science, Research and Innovation Fund (NSRF), Thailand; Turkish Energy, Nuclear and Mineral Research Agency (TENMAK), Turkey; National Academy of Sciences of Ukraine, Ukraine; Science and Technology Facilities Council (STFC), United Kingdom; National Science Foundation of the United States of America (NSF) and United States Department of Energy, Office of Nuclear Physics (DOE NP), United States of America. In addition, individual groups or members have received support from: Marie Skłodowska Curie, European Research Council, Strong 2020 - Horizon 2020 (grant nos. 950692, 824093, 896850), European Union; Academy of Finland (Center of Excellence in Quark Matter) (grant nos. 346327, 346328), Finland; Programa de Apoyos para la Superación del Personal Académico, UNAM, Mexico.

References

- [1] W. Busza, K. Rajagopal, and W. van der Schee, “Heavy Ion Collisions: The Big Picture, and the Big Questions”, *Ann. Rev. Nucl. Part. Sci.* **68** (2018) 339–376, arXiv:1802.04801 [hep-ph].
- [2] U. Heinz and R. Snellings, “Collective flow and viscosity in relativistic heavy-ion collisions”, *Ann. Rev. Nucl. Part. Sci.* **63** (2013) 123–151, arXiv:1301.2826 [nucl-th].
- [3] J. E. Bernhard, J. S. Moreland, S. A. Bass, J. Liu, and U. Heinz, “Applying Bayesian parameter estimation to relativistic heavy-ion collisions: Simultaneous characterization of the initial state and quark-gluon plasma medium”, *Phys. Rev.* **C94** (2016) 024907, arXiv:1605.03954 [nucl-th].
- [4] F. G. Gardim, G. Giacalone, M. Luzum, and J.-Y. Ollitrault, “Thermodynamics of hot strong-interaction matter from ultrarelativistic nuclear collisions”, *Nature Phys.* **16** (2020) 615–619, arXiv:1908.09728 [nucl-th].
- [5] A. Andronic, P. Braun-Munzinger, K. Redlich, and J. Stachel, “Decoding the phase structure of QCD via particle production at high energy”, *Nature* **561** (2018) 321–330, arXiv:1710.09425 [nucl-th].
- [6] P. Braun-Munzinger, K. Redlich, and J. Stachel, “Particle production in heavy ion collisions”, in *Quark Gluon Plasma 3*, R. C. Hwa and X.N. Wang, ed., pp. 491–599. World Scientific, Singapore, 2003. arXiv:nucl-th/0304013 [nucl-th].
- [7] **ALICE** Collaboration, J. Adam *et al.*, “Centrality dependence of the nuclear modification factor of charged pions, kaons, and protons in Pb–Pb collisions at $\sqrt{s_{\text{NN}}} = 2.76$ TeV”, *Phys. Rev. C* **93** (2016) 034913, arXiv:1506.07287 [nucl-ex].
- [8] **ALICE** Collaboration, S. Acharya *et al.*, “Transverse momentum spectra and nuclear modification factors of charged particles in pp, p–Pb and Pb–Pb collisions at the LHC”, *JHEP* **11** (2018) 013, arXiv:1802.09145 [nucl-ex].
- [9] **ALICE** Collaboration, J. Adam *et al.*, “Multiplicity dependence of charged pion, kaon, and (anti)proton production at large transverse momentum in p–Pb collisions at $\sqrt{s_{\text{NN}}} = 5.02$ TeV”, *Phys. Lett.* **B760** (2016) 720–735, arXiv:1601.03658 [nucl-ex].
- [10] **ALICE** Collaboration, B. Abelev *et al.*, “Long-range angular correlations of π , K and p in p–Pb collisions at $\sqrt{s_{\text{NN}}} = 5.02$ TeV”, *Phys. Lett. B* **726** (2013) 164–177, arXiv:1307.3237 [nucl-ex].
- [11] **CMS** Collaboration, V. Khachatryan *et al.*, “Long-range two-particle correlations of strange hadrons with charged particles in pPb and PbPb collisions at LHC energies”, *Phys. Lett.* **B742** (2015) 200–224, arXiv:1409.3392 [nucl-ex].
- [12] **CMS** Collaboration, S. Chatrchyan *et al.*, “Multiplicity and transverse-momentum dependence of two- and four-particle correlations in pPb and PbPb collisions”, *Phys. Lett. B* **724** (2013) 213–240, arXiv:1305.0609 [nucl-ex].
- [13] **CMS** Collaboration, V. Khachatryan *et al.*, “Evidence for Collective Multiparticle Correlations in p–Pb Collisions”, *Phys. Rev. Lett.* **115** (2015) 012301, arXiv:1502.05382 [nucl-ex].
- [14] **ATLAS** Collaboration, G. Aad *et al.*, “Measurement with the ATLAS detector of multi-particle azimuthal correlations in p+Pb collisions at $\sqrt{s_{\text{NN}}} = 5.02$ TeV”, *Phys. Lett. B* **725** (2013) 60–78, arXiv:1303.2084 [hep-ex].

- [15] K. Dusling and R. Venugopalan, “Comparison of the color glass condensate to dihadron correlations in proton-proton and proton-nucleus collisions”, *Phys. Rev. D* **87** (2013) 094034, arXiv:1302.7018 [hep-ph].
- [16] B. Blok, C. D. Jakel, M. Strikman, and U. A. Wiedemann, “Collectivity from interference”, *JHEP* **12** (2017) 074, arXiv:1708.08241 [hep-ph].
- [17] B. Schenke, “The smallest fluid on Earth”, *Rept. Prog. Phys.* **84** (2021) 082301, arXiv:2102.11189 [nucl-th].
- [18] J. E. Bernhard, J. S. Moreland, and S. A. Bass, “Bayesian estimation of the specific shear and bulk viscosity of quark–gluon plasma”, *Nature Phys.* **15** (2019) 1113–1117.
- [19] J. S. Moreland, J. E. Bernhard, and S. A. Bass, “Bayesian calibration of a hybrid nuclear collision model using p-Pb and Pb-Pb data at energies available at the CERN Large Hadron Collider”, *Phys. Rev. C* **101** (2020) 024911, arXiv:1808.02106 [nucl-th].
- [20] B. Schenke, C. Shen, and P. Tribedy, “Running the gamut of high energy nuclear collisions”, *Phys. Rev. C* **102** (2020) 044905, arXiv:2005.14682 [nucl-th].
- [21] K. Dusling, W. Li, and B. Schenke, “Novel collective phenomena in high-energy proton–proton and proton–nucleus collisions”, *Int. J. Mod. Phys. E* **25** (2016) 1630002, arXiv:1509.07939 [nucl-ex].
- [22] L. McLerran, M. Praszalowicz, and B. Schenke, “Transverse momentum of protons, pions and kaons in high multiplicity pp and pA collisions: Evidence for the color glass condensate?”, *Nucl. Phys.* **A916** (2013) 210–218, arXiv:1306.2350 [hep-ph].
- [23] T. Sjöstrand, S. Ask, J. R. Christiansen, R. Corke, N. Desai, P. Ilten, S. Mrenna, S. Prestel, C. O. Rasmussen, and P. Z. Skands, “An Introduction to PYTHIA 8.2”, *Comput. Phys. Commun.* **191** (2015) 159–177, arXiv:1410.3012 [hep-ph].
- [24] P. Z. Skands, “Tuning Monte Carlo generators: The Perugia tunes”, *Phys. Rev. D* **82** (2010) 074018, arXiv:1005.3457 [hep-ph].
- [25] C. Bierlich, G. Gustafson, and L. Lönnblad, “Collectivity without plasma in hadronic collisions”, *Phys. Lett.* **B779** (2018) 58–63, arXiv:1710.09725 [hep-ph].
- [26] C. Bierlich, G. Gustafson, L. Lönnblad, and H. Shah, “The Angantyr model for heavy-ion collisions in PYTHIA8”, *JHEP* **10** (2018) 134, arXiv:1806.10820 [hep-ph].
- [27] H. J. Drescher, M. Hladik, S. Ostapchenko, T. Pierog, and K. Werner, “Parton based Gribov-Regge theory”, *Phys. Rept.* **350** (2001) 93–289, arXiv:hep-ph/0007198 [hep-ph].
- [28] K. Werner, B. Guiot, I. Karpenko, T. Pierog, G. Sophys, and M. Stefaniak, “EPOS”, *EPJ Web Conf.* **208** (2019) 11005.
- [29] K. Werner, B. Guiot, I. Karpenko, and T. Pierog, “Analysing radial flow features in p-Pb and p-p collisions at several TeV by studying identified particle production in EPOS3”, *Phys. Rev.* **C89** (2014) 064903, arXiv:1312.1233 [nucl-th].
- [30] T. Pierog, I. Karpenko, J. M. Katzy, E. Yatsenko, and K. Werner, “EPOS LHC: Test of collective hadronization with data measured at the CERN Large Hadron Collider”, *Phys. Rev. C* **92** (2015) 034906, arXiv:1306.0121 [hep-ph].















- [31] P. Skands, S. Carrazza, and J. Rojo, “Tuning PYTHIA 8.1: the Monash 2013 tune”, *Eur. Phys. J.* **C74** (2014) 3024, arXiv:1404.5630 [hep-ph].
- [32] UA1 Collaboration, G. Arnison *et al.*, “Transverse momentum spectra for charged particles at the CERN proton-antiproton collider”, *Phys. Lett. B* **118** (1982) 167.
- [33] ABCDHW Collaboration, A. Breakstone *et al.*, “Multiplicity dependence of the average transverse momentum and of the particle source size in p-p interactions at $\sqrt{s} = 62, 44$ and 31 GeV”, *Z. f. Physik C* **33(3)** (1987) 333.
- [34] UA1 Collaboration, C. Albajar *et al.*, “A study of the general characteristics of proton-antiproton collisions at $\sqrt{s} = 0.2$ TeV to 0.9 TeV”, *Nucl. Phys. B* **335** (1990) 261.
- [35] E735 Collaboration, T. Alexopoulos *et al.*, “Multiplicity dependence of the transverse-momentum spectrum for centrally produced hadrons in antiproton-proton collisions at $\sqrt{s} = 1.8$ TeV”, *Phys. Rev. Lett.* **60** (Apr, 1988) 1622–1625.
- [36] STAR Collaboration, J. Adams *et al.*, “The Multiplicity dependence of inclusive p_T spectra from pp collisions at $\sqrt{s} = 200$ GeV”, *Phys. Rev. D* **74** (2006) 032006, arXiv:nucl-ex/0606028 [nucl-ex].
- [37] CDF Collaboration, T. Aaltonen *et al.*, “Measurement of particle production and inclusive differential cross sections in $p\bar{p}$ collisions at $\sqrt{s} = 1.96$ TeV”, *Phys. Rev. D* **79** (2009) 112005, arXiv:0904.1098 [hep-ex].
- [38] ALICE Collaboration, K. Aamodt *et al.*, “Transverse momentum spectra of charged particles in proton-proton collisions at $\sqrt{s} = 900$ GeV with ALICE at the LHC”, *Phys. Lett. B* **693** (2010) 53–68, arXiv:1007.0719 [hep-ex].
- [39] CMS Collaboration, V. Khachatryan *et al.*, “Charged particle multiplicities in pp interactions at $\sqrt{s} = 0.9, 2.36,$ and 7 TeV”, *JHEP* **01** (2011) 079, arXiv:1011.5531 [hep-ex].
- [40] ATLAS Collaboration, G. Aad *et al.*, “Charged-particle multiplicities in pp interactions measured with the ATLAS detector at the LHC”, *New J. Phys.* **13** (2011) 053033, arXiv:1012.5104 [hep-ex].
- [41] ALICE Collaboration, J. Adam *et al.*, “Pseudorapidity and transverse-momentum distributions of charged particles in proton-proton collisions at $\sqrt{s} = 13$ TeV”, *Phys. Lett.* **B753** (2016) 319–329, arXiv:1509.08734 [nucl-ex].
- [42] ALICE Collaboration, S. Acharya *et al.*, “Transverse momentum spectra and nuclear modification factors of charged particles in Xe–Xe collisions at $\sqrt{s_{NN}} = 5.44$ TeV”, *Phys. Lett.* **B788** (2019) 166–179, arXiv:1805.04399 [nucl-ex].
- [43] J. R. Christiansen and P. Z. Skands, “String formation beyond leading colour”, *JHEP* **08** (2015) 003, arXiv:1505.01681 [hep-ph].
- [44] L. McLerran and M. Praszalowicz, “Geometrical scaling and the dependence of the average transverse momentum on the multiplicity and energy for the ALICE experiment”, *Phys. Lett.* **B741** (2015) 246–251, arXiv:1407.6687 [hep-ph].
- [45] ALICE Collaboration, K. Aamodt *et al.*, “The ALICE experiment at the CERN LHC”, *JINST* **3** (2008) S08002.
- [46] ALICE Collaboration, B. Abelev *et al.*, “Performance of the ALICE experiment at the CERN LHC”, *Int. J. Mod. Phys. A* **29** (2014) 1430044, arXiv:1402.4476 [nucl-ex].

- [47] **ALICE** Collaboration, K. Aamodt *et al.*, “Alignment of the ALICE Inner Tracking System with cosmic-ray tracks”, *JINST* **5** (2010) P03003, arXiv:1001.0502 [physics.ins-det].
- [48] J. Alme, Y. Andres, H. Appelshauer, S. Bablok, N. Bialas, *et al.*, “The ALICE TPC, a large 3-dimensional tracking device with fast readout for ultra-high multiplicity events”, *Nucl. Instrum. Meth. A* **622** (2010) 316–367, arXiv:1001.1950 [physics.ins-det].
- [49] **ALICE** Collaboration, S. Acharya *et al.*, “Centrality and pseudorapidity dependence of the charged-particle multiplicity density in Xe–Xe collisions at $\sqrt{s_{NN}}=5.44\text{TeV}$ ”, *Phys. Lett. B* **790** (2019) 35–48, arXiv:1805.04432 [nucl-ex].
- [50] **ALICE** Collaboration, S. Acharya *et al.*, “The ALICE definition of primary particles”, *ALICE-PUBLIC-2017-005* (Jun, 2017). <https://cds.cern.ch/record/2270008>.
- [51] R. Brun *et al.*, “GEANT: Detector Description and Simulation Tool”, *CERN-W5013* (1994).
- [52] **ALICE** Collaboration, J. Adam *et al.*, “Enhanced production of multi-strange hadrons in high-multiplicity proton-proton collisions”, *Nature Phys.* **13** (2017) 535–539, arXiv:1606.07424 [nucl-ex].
- [53] **ALICE** Collaboration, S. Acharya *et al.*, “Multiplicity dependence of π , K, and p production in pp collisions at $\sqrt{s} = 13\text{ TeV}$ ”, *Eur. Phys. J. C* **80** (2020) 693, arXiv:2003.02394 [nucl-ex].
- [54] **ALICE** Collaboration, S. Acharya *et al.*, “Multiplicity dependence of (multi-)strange hadron production in proton-proton collisions at $\sqrt{s} = 13\text{ TeV}$ ”, *Eur. Phys. J. C* **80** (2020) 167, arXiv:1908.01861 [nucl-ex].
- [55] **ALICE** Collaboration, B. Abelev *et al.*, “Multiplicity Dependence of Pion, Kaon, Proton and Lambda Production in p-Pb Collisions at $\sqrt{s_{NN}} = 5.02\text{ TeV}$ ”, *Phys. Lett. B* **728** (2014) 25–38, arXiv:1307.6796 [nucl-ex].
- [56] **ALICE** Collaboration, B. Abelev *et al.*, “Centrality dependence of π , K, p production in Pb-Pb collisions at $\sqrt{s_{NN}} = 2.76\text{ TeV}$ ”, *Phys. Rev. C* **88** (2013) 044910, arXiv:1303.0737 [hep-ex].
- [57] G. D’Agostini, “A Multidimensional unfolding method based on Bayes’ theorem”, *Nucl. Instrum. Meth.* **A362** (1995) 487–498.
- [58] T. Auye, “Unfolding algorithms and tests using RooUnfold”, *Proceedings of the PHYSTAT 2011 Workshop, CERN, Geneva, Switzerland, January 2011*, **CERN-2011-006** 313–318, arXiv:1105.1160 [physics.data-an].
- [59] X.-N. Wang and M. Gyulassy, “HIJING: A Monte Carlo model for multiple jet production in pp, pA and AA collisions”, *Phys. Rev. D* **44** (1991) 3501–3516. (HIJING v1.383).
- [60] **ALICE** Collaboration, S. Acharya *et al.*, “Charged-particle production as a function of multiplicity and transverse sphericity in pp collisions at $\sqrt{s} = 5.02$ and 13 TeV ”, *Eur. Phys. J. C* **79** (2019) 857, arXiv:1905.07208 [nucl-ex].
- [61] Z. Koba, H. B. Nielsen, and P. Olesen, “Scaling of multiplicity distributions in high energy hadron collisions”, *Nucl. Phys. B* **40** (1972) 317–334.
- [62] **ALICE** Collaboration, B. Abelev *et al.*, “Multiplicity dependence of the average transverse momentum in pp, p–Pb, and Pb–Pb collisions at the LHC”, *Physics Letters B* **727** (Dec, 2013) 371–380, arXiv:1307.1094 [nucl-ex].

- [63] G. Giacalone, J. Noronha-Hostler, M. Luzum, and J.-Y. Ollitrault, “Hydrodynamic predictions for 5.44 TeV Xe+Xe collisions”, *Phys. Rev. C* **97** (Mar, 2018) 034904, arXiv:1711.08499 [nucl-th].
- [64] C. Bierlich, S. Chakraborty, G. Gustafson, and L. Lönnblad, “Setting the string shoving picture in a new frame”, *JHEP* **03** (2021) 270, arXiv:2010.07595 [hep-ph].
- [65] A. Bzdak, B. Schenke, P. Tribedy, and R. Venugopalan, “Initial-state geometry and the role of hydrodynamics in proton-proton, proton-nucleus, and deuteron-nucleus collisions”, *Phys. Rev. C* **87** (Jun, 2013) 064906.
- [66] M. Praszalowicz and A. Francuz, “Geometrical scaling in inelastic inclusive particle production at the LHC”, *Phys. Rev. D* **92** (Oct, 2015), arXiv:1507.08186 [hep-ph].
- [67] M. Petrovici, A. Lindner, A. Pop, M. Târzila, and I. Berceanu, “Geometrical scaling for energies available at the BNL Relativistic Heavy Ion Collider to those at the CERN Large Hadron Collider”, *Phys. Rev. C* **98** (2018) 024904, arXiv:1805.04060 [hep-ph].

W. Guo⁶, A. Gupta⁹⁰, R. Gupta⁹⁰, S.P. Guzman⁴⁴, L. Gyulai¹³⁶, M.K. Habib⁹⁶, C. Hadjidakis¹²⁸, F.U. Haider⁹⁰, H. Hamagaki⁷⁵, A. Hamdi⁷³, M. Hamid⁶, Y. Han¹³⁸, R. Hannigan¹⁰⁷, M.R. Haque¹³³, J.W. Harris¹³⁷, A. Harton⁹, H. Hassan⁸⁶, D. Hatzifotiadou⁵⁰, P. Hauer⁴², L.B. Havener¹³⁷, S.T. Heckel⁹⁴, E. Hellbär⁹⁶, H. Helstrup³⁴, M. Hemmer⁶³, T. Herman³⁵, G. Herrera Corral⁸, F. Herrmann¹³⁵, S. Herrmann¹²⁵, K.F. Hetland³⁴, B. Heybeck⁶³, H. Hillemanns³², C. Hills¹¹⁶, B. Hippolyte¹²⁶, F.W. Hoffmann⁶⁹, B. Hofman⁵⁸, B. Hohlweger⁸³, G.H. Hong¹³⁸, M. Horst⁹⁴, A. Horzyk², R. Hosokawa¹⁴, Y. Hou⁶, P. Hristov³², C. Hughes¹¹⁹, P. Huhn⁶³, L.M. Huhta¹¹⁴, C.V. Hulse¹²⁸, T.J. Humanic⁸⁷, A. Hutson¹¹³, D. Hutter³⁸, J.P. Iddon¹¹⁶, R. Ilkaev¹⁴⁰, H. Ilyas¹³, M. Inaba¹²², G.M. Innocenti³², M. Ippolito¹⁴⁰, A. Isakov⁸⁵, T. Isidori¹¹⁵, M.S. Islam⁹⁸, M. Ivanov⁹⁶, M. Ivanov¹², V. Ivanov¹⁴⁰, M. Jablonski², B. Jacak⁷³, N. Jacazio³², P.M. Jacobs⁷³, S. Jadlovská¹⁰⁵, J. Jadlovsky¹⁰⁵, S. Jaelani⁸¹, L. Jaffe³⁸, C. Jahnke¹¹⁰, M.J. Jakubowska¹³³, M.A. Janik¹³³, T. Janson⁶⁹, M. Jercic⁸⁸, S. Jia¹⁰, A.A.P. Jimenez⁶⁴, F. Jonas⁸⁶, J.M. Jowett^{32,96}, J. Jung⁶³, M. Jung⁶³, A. Junique³², A. Jusko⁹⁹, M.J. Kabus^{32,133}, J. Kaewjai¹⁰⁴, P. Kalinak⁵⁹, A.S. Kalteyer⁹⁶, A. Kalweit³², V. Kaplin¹⁴⁰, A. Karasu Uysal⁷¹, D. Karatovic⁸⁸, O. Karavichev¹⁴⁰, T. Karavicheva¹⁴⁰, P. Karczmarczyk¹³³, E. Karpechev¹⁴⁰, U. Keschull⁶⁹, R. Keidel¹³⁹, D.L.D. Keijdener⁵⁸, M. Keil³², B. Ketzer⁴², A.M. Khan⁶, S. Khan¹⁵, A. Khanzadeev¹⁴⁰, Y. Kharlov¹⁴⁰, A. Khatun^{115,15}, A. Khuntia¹⁰⁶, M.B. Kidson¹¹², B. Kileng³⁴, B. Kim¹⁶, C. Kim¹⁶, D.J. Kim¹¹⁴, E.J. Kim⁶⁸, J. Kim¹³⁸, J.S. Kim⁴⁰, J. Kim⁶⁸, M. Kim^{18,93}, S. Kim¹⁷, T. Kim¹³⁸, K. Kimura⁹¹, S. Kirsch⁶³, I. Kisel³⁸, S. Kiselev¹⁴⁰, A. Kisiel¹³³, J.P. Kitowski², J.L. Klay⁵, J. Klein³², S. Klein⁷³, C. Klein-Bösing¹³⁵, M. Kleiner⁶³, T. Klemenz⁹⁴, A. Kluge³², A.G. Knospe¹¹³, C. Kobdaj¹⁰⁴, T. Kollegger⁹⁶, A. Kondratyev¹⁴¹, N. Kondratyeva¹⁴⁰, E. Kondratyuk¹⁴⁰, J. König⁶³, S.A. Königstorfer⁹⁴, P.J. Konopka³², G. Kornakov¹³³, S.D. Koryciak², A. Kotliarov⁸⁵, V. Kovalenko¹⁴⁰, M. Kowalski¹⁰⁶, V. Kozuharov³⁶, I. Králik⁵⁹, A. Kravčáková³⁷, L. Kreis⁹⁶, M. Krivda^{99,59}, F. Krizek⁸⁵, K. Krizkova Gajdosova³⁵, M. Kroesen⁹³, M. Krüger⁶³, D.M. Krupova³⁵, E. Kryshen¹⁴⁰, V. Kucera³², C. Kuhn¹²⁶, P.G. Kuijer⁸³, T. Kumaoka¹²², D. Kumar¹³², L. Kumar⁸⁹, N. Kumar⁸⁹, S. Kumar³¹, S. Kundu³², P. Kurashvili⁷⁸, A. Kurepin¹⁴⁰, A.B. Kurepin¹⁴⁰, A. Kuryakin¹⁴⁰, S. Kuschpil⁸⁵, J. Kvapil⁹⁹, M.J. Kweon⁵⁷, J.Y. Kwon⁵⁷, Y. Kwon¹³⁸, S.L. La Pointe³⁸, P. La Rocca²⁶, Y.S. Lal⁷³, A. Lakrathok¹⁰⁴, M. Lamanna³², R. Langoy¹¹⁸, P. Larionov³², E. Laudi³², L. Lautner^{32,94}, R. Lavicka¹⁰¹, T. Lazareva¹⁴⁰, R. Lea^{131,54}, H. Lee¹⁰³, G. Legras¹³⁵, J. Lehrbach³⁸, R.C. Lemmon⁸⁴, I. León Monzón¹⁰⁸, M.M. Lesch⁹⁴, E.D. Lesser¹⁸, M. Lettrich⁹⁴, P. Lévai¹³⁶, X. Li¹⁰, X.L. Li⁶, J. Lien¹¹⁸, R. Lietava⁹⁹, I. Likmeta¹¹³, B. Lim^{24,16}, S.H. Lim¹⁶, V. Lindenstruth³⁸, A. Lindner⁴⁵, C. Lippmann⁹⁶, A. Liu¹⁸, D.H. Liu⁶, J. Liu¹¹⁶, I.M. Lofnes²⁰, C. Loizides⁸⁶, S. Lokos¹⁰⁶, J. Lomker⁵⁸, P. Loncar³³, J.A. Lopez⁹³, X. Lopez¹²⁴, E. López Torres⁷, P. Lu^{96,117}, J.R. Luhder¹³⁵, M. Lunardon²⁷, G. Luparello⁵⁶, Y.G. Ma³⁹, A. Maevskaya¹⁴⁰, M. Mager³², T. Mahmoud⁴², A. Maire¹²⁶, M.V. Makariev³⁶, M. Malaev¹⁴⁰, G. Malfattore²⁵, N.M. Malik⁹⁰, Q.W. Malik¹⁹, S.K. Malik⁹⁰, L. Malinina^{VII,141}, D. Mal'Kevich¹⁴⁰, D. Mallick⁷⁹, N. Mallick⁴⁷, G. Mandaglio^{30,52}, V. Manko¹⁴⁰, F. Manso¹²⁴, V. Manzari⁴⁹, Y. Mao⁶, G.V. Margagliotti²³, A. Margotti⁵⁰, A. Marín⁹⁶, C. Markert¹⁰⁷, P. Martinengo³², J.L. Martinez¹¹³, M.I. Martínez⁴⁴, G. Martínez García¹⁰², S. Masciocchi⁹⁶, M. Masera²⁴, A. Masoni⁵¹, L. Massacrier¹²⁸, A. Mastroserio^{129,49}, O. Matonoha⁷⁴, P.F.T. Matuoka¹⁰⁹, A. Matyja¹⁰⁶, C. Mayer¹⁰⁶, A.L. Mazuecos³², F. Mazzaschi²⁴, M. Mazzilli³², J.E. Mdhului¹²⁰, A.F. Mechler⁶³, Y. Melikyan^{43,140}, A. Menchaca-Rocha⁶⁶, E. Meninno^{101,28}, A.S. Menon¹¹³, M. Meres¹², S. Mhlanga^{112,67}, Y. Miake¹²², L. Micheletti⁵⁵, L.C. Migliorin¹²⁵, D.L. Mihaylov⁹⁴, K. Mikhaylov^{141,140}, A.N. Mishra¹³⁶, D. Miśkowiec⁹⁶, A. Modak⁴, A.P. Mohanty⁵⁸, B. Mohanty⁷⁹, M. Mohisin Khan^{V,15}, M.A. Molander⁴³, Z. Moravcova⁸², C. Mordasini⁹⁴, D.A. Moreira De Godoy¹³⁵, I. Morozov¹⁴⁰, A. Morsch³², T. Mrnjavac³², V. Muccifora⁴⁸, S. Muhuri¹³², J.D. Mulligan⁷³, A. Mulliri²², M.G. Munhoz¹⁰⁹, R.H. Munzer⁶³, H. Murakami¹²¹, S. Murray¹¹², L. Musa³², J. Musinsky⁵⁹, J.W. Myrcha¹³³, B. Naik¹²⁰, A.I. Nambrath¹⁸, B.K. Nandi⁴⁶, R. Nania⁵⁰, E. Nappi⁴⁹, A.F. Nassirpour⁷⁴, A. Nath⁹³, C. Natrass¹¹⁹, M.N. Naydenov³⁶, A. Neagu¹⁹, A. Negru¹²³, L. Nellen⁶⁴, S.V. Nesbo³⁴, G. Neskovic³⁸, D. Nesterov¹⁴⁰, B.S. Nielsen⁸², E.G. Nielsen⁸², S. Nikolaev¹⁴⁰, S. Nikulin¹⁴⁰, V. Nikulin¹⁴⁰, F. Noferini⁵⁰, S. Noh¹¹, P. Nomokonov¹⁴¹, J. Norman¹¹⁶, N. Novitzky¹²², P. Nowakowski¹³³, A. Nyanin¹⁴⁰, J. Nystrand²⁰, M. Ogino⁷⁵, A. Ohlson⁷⁴, V.A. Okorokov¹⁴⁰, J. Oleniacz¹³³, A.C. Oliveira Da Silva¹¹⁹, M.H. Oliver¹³⁷, A. Onnerstad¹¹⁴, C. Oppedisano⁵⁵, A. Ortiz Velasquez⁶⁴, J. Otwinowski¹⁰⁶, M. Oya⁹¹, K. Oyama⁷⁵, Y. Pachmayer⁹³, S. Padhan⁴⁶, D. Pagano^{131,54}, G. Paic⁶⁴, A. Palasciano⁴⁹, S. Panebianco¹²⁷,

H. Park ¹²², H. Park ¹⁰³, J. Park ⁵⁷, J.E. Parkkila ³², R.N. Patra⁹⁰, B. Paul ²², H. Pei ⁶,
T. Peitzmann ⁵⁸, X. Peng ⁶, M. Pennisi ²⁴, L.G. Pereira ⁶⁵, D. Peresunko ¹⁴⁰, G.M. Perez ⁷,
S. Perrin ¹²⁷, Y. Pestov¹⁴⁰, V. Petráček ³⁵, V. Petrov ¹⁴⁰, M. Petrovici ⁴⁵, R.P. Pezzi ^{102,65}, S. Piano ⁵⁶,
M. Pikna ¹², P. Pillot ¹⁰², O. Pinazza ^{50,32}, L. Pinsky¹¹³, C. Pinto ⁹⁴, S. Pisano ⁴⁸, M. Płoskoń ⁷³,
M. Planinic⁸⁸, F. Pliquett⁶³, M.G. Poghosyan ⁸⁶, B. Polichtchouk ¹⁴⁰, S. Politano ²⁹, N. Poljak ⁸⁸,
A. Pop ⁴⁵, S. Porteboeuf-Houssais ¹²⁴, V. Pozdniakov ¹⁴¹, K.K. Pradhan ⁴⁷, S.K. Prasad ⁴,
S. Prasad ⁴⁷, R. Preghenella ⁵⁰, F. Prino ⁵⁵, C.A. Pruneau ¹³⁴, I. Pshenichnov ¹⁴⁰, M. Puccio ³²,
S. Pucillo ²⁴, Z. Pugelova¹⁰⁵, S. Qiu ⁸³, L. Quaglia ²⁴, R.E. Quishpe¹¹³, S. Ragoni ^{14,99},
A. Rakotozafindrabe ¹²⁷, L. Ramello ^{130,55}, F. Rami ¹²⁶, S.A.R. Ramirez ⁴⁴, T.A. Rancien⁷², M. Rasa ²⁶,
S.S. Räsänen ⁴³, R. Rath ⁵⁰, M.P. Rauch ²⁰, I. Ravasenga ⁸³, K.F. Read ^{86,119}, C. Reckziegel ¹¹¹,
A.R. Redelbach ³⁸, K. Redlich ^{VI,78}, C.A. Reetz ⁹⁶, A. Rehman²⁰, F. Reidt ³², H.A. Reme-Ness ³⁴,
Z. Rescakova³⁷, K. Reygers ⁹³, A. Riabov ¹⁴⁰, V. Riabov ¹⁴⁰, R. Ricci ²⁸, M. Richter ¹⁹,
A.A. Riedel ⁹⁴, W. Riegler ³², C. Ristea ⁶², M. Rodríguez Cahuantzi ⁴⁴, K. Røed ¹⁹, R. Rogalev ¹⁴⁰,
E. Rogochaya ¹⁴¹, T.S. Rogoschinski ⁶³, D. Rohr ³², D. Röhrich ²⁰, P.F. Rojas⁴⁴, S. Rojas Torres ³⁵,
P.S. Rokita ¹³³, G. Romanenko ¹⁴¹, F. Ronchetti ⁴⁸, A. Rosano ^{30,52}, E.D. Rosas⁶⁴, K. Roslon ¹³³,
A. Rossi ⁵³, A. Roy ⁴⁷, S. Roy ⁴⁶, N. Rubini ²⁵, D. Ruggiano ¹³³, R. Rui ²³, B. Rumyantsev¹⁴¹,
P.G. Russek ², R. Russo ⁸³, A. Rustamov ⁸⁰, E. Ryabinkin ¹⁴⁰, Y. Ryabov ¹⁴⁰, A. Rybicki ¹⁰⁶,
H. Rytkonen ¹¹⁴, W. Rzesza ¹³³, O.A.M. Saarimaki ⁴³, R. Sadek ¹⁰², S. Sadhu ³¹, S. Sadovsky ¹⁴⁰,
J. Saetre ²⁰, K. Safarik ³⁵, S.K. Saha ⁴, S. Saha ⁷⁹, B. Sahoo ⁴⁶, R. Sahoo ⁴⁷, S. Sahoo⁶⁰, D. Sahu ⁴⁷,
P.K. Sahu ⁶⁰, J. Saini ¹³², K. Sajdakova³⁷, S. Sakai ¹²², M.P. Salvan ⁹⁶, S. Sambyal ⁹⁰, I. Sanna ^{32,94},
T.B. Saramela¹⁰⁹, D. Sarkar ¹³⁴, N. Sarkar¹³², P. Sarma ⁴¹, V. Sarritzu ²², V.M. Sarti ⁹⁴, M.H.P. Sas ¹³⁷,
J. Schambach ⁸⁶, H.S. Scheid ⁶³, C. Schiaua ⁴⁵, R. Schicker ⁹³, A. Schmah⁹³, C. Schmidt ⁹⁶,
H.R. Schmidt⁹², M.O. Schmidt ³², M. Schmidt⁹², N.V. Schmidt ⁸⁶, A.R. Schmier ¹¹⁹, R. Schotter ¹²⁶,
A. Schröter ³⁸, J. Schukraft ³², K. Schwarz⁹⁶, K. Schweda ⁹⁶, G. Scioli ²⁵, E. Scomparin ⁵⁵,
J.E. Seger ¹⁴, Y. Sekiguchi¹²¹, D. Sekihata ¹²¹, I. Selyuzhenkov ^{96,140}, S. Senyukov ¹²⁶, J.J. Seo ⁵⁷,
D. Serebryakov ¹⁴⁰, L. Serksnyte ⁹⁴, A. Sevcenco ⁶², T.J. Shaba ⁶⁷, A. Shabetai ¹⁰², R. Shahoyan³²,
A. Shangaraev ¹⁴⁰, A. Sharma⁸⁹, B. Sharma ⁹⁰, D. Sharma ⁴⁶, H. Sharma ¹⁰⁶, M. Sharma ⁹⁰,
S. Sharma ⁷⁵, S. Sharma ⁹⁰, U. Sharma ⁹⁰, A. Shatat ¹²⁸, O. Sheibani¹¹³, K. Shigaki ⁹¹,
M. Shimomura⁷⁶, J. Shin¹¹, S. Shirinkin ¹⁴⁰, Q. Shou ³⁹, Y. Sibiriak ¹⁴⁰, S. Siddhanta ⁵¹,
T. Siemiarczuk ⁷⁸, T.F. Silva ¹⁰⁹, D. Silvermyr ⁷⁴, T. Simantathammakul¹⁰⁴, R. Simeonov ³⁶, B. Singh⁹⁰,
B. Singh ⁹⁴, R. Singh ⁷⁹, R. Singh ⁹⁰, R. Singh ⁴⁷, S. Singh ¹⁵, V.K. Singh ¹³², V. Singhal ¹³²,
T. Sinha ⁹⁸, B. Sitar ¹², M. Sitta ^{130,55}, T.B. Skaali¹⁹, G. Skorodumovs ⁹³, M. Slupecki ⁴³,
N. Smirnov ¹³⁷, R.J.M. Snellings ⁵⁸, E.H. Solheim ¹⁹, J. Song ¹¹³, A. Songmoolnak¹⁰⁴, F. Soramel ²⁷,
R. Spijkers ⁸³, I. Sputowska ¹⁰⁶, J. Staa ⁷⁴, J. Stachel ⁹³, I. Stan ⁶², P.J. Steffanic ¹¹⁹,
S.F. Stiefelmaier ⁹³, D. Stocco ¹⁰², I. Storehaug ¹⁹, P. Stratmann ¹³⁵, S. Strazzi ²⁵, C.P. Stylianidis⁸³,
A.A.P. Suaide ¹⁰⁹, C. Suire ¹²⁸, M. Sukhanov ¹⁴⁰, M. Suljic ³², R. Sultanov ¹⁴⁰, V. Sumberia ⁹⁰,
S. Sumowidagdo ⁸¹, S. Swain⁶⁰, I. Szarka ¹², M. Szymkowski ¹³³, S.F. Taghavi ⁹⁴, G. TAILLEPIED ⁹⁶,
J. Takahashi ¹¹⁰, G.J. Tambave ²⁰, S. Tang ^{124,6}, Z. Tang ¹¹⁷, J.D. Tapia Takaki ¹¹⁵, N. Tapus¹²³,
L.A. Tarasovicova ¹³⁵, M.G. Tarzila ⁴⁵, G.F. Tassielli ³¹, A. Tauro ³², G. Tejada Muñoz ⁴⁴,
A. Telesca ³², L. Terlizzi ²⁴, C. Terrevoli ¹¹³, G. Tersimonov³, S. Thakur ⁴, D. Thomas ¹⁰⁷,
A. Tikhonov ¹⁴⁰, A.R. Timmins ¹¹³, M. Tkacik¹⁰⁵, T. Tkacik ¹⁰⁵, A. Toia ⁶³, R. Tokumoto⁹¹,
N. Topilskaya ¹⁴⁰, M. Toppi ⁴⁸, F. Torales-Acosta¹⁸, T. Tork ¹²⁸, A.G. Torres Ramos ³¹, A. Trifiró ^{30,52},
A.S. Triolo ^{30,52}, S. Tripathy ⁵⁰, T. Tripathy ⁴⁶, S. Trogolo ³², V. Trubnikov ³, W.H. Trzaska ¹¹⁴,
T.P. Trzcinski ¹³³, A. Tumkin ¹⁴⁰, R. Turrisi ⁵³, T.S. Tveter ¹⁹, K. Ullaland ²⁰, B. Ulukutlu ⁹⁴,
A. Uras ¹²⁵, M. Urioni ^{54,131}, G.L. Usai ²², M. Vala³⁷, N. Valle ²¹, L.V.R. van Doremalen⁵⁸, M. van
Leeuwen ⁸³, C.A. van Veen ⁹³, R.J.G. van Weelden ⁸³, P. Vande Vyvre ³², D. Varga ¹³⁶, Z. Varga ¹³⁶,
M. Vasileiou ⁷⁷, A. Vasiliev ¹⁴⁰, O. Vázquez Doce ⁴⁸, O. Vazquez Rueda ^{113,74}, V. Vechernin ¹⁴⁰,
E. Vercellin ²⁴, S. Vergara Limón⁴⁴, L. Vermunt ⁹⁶, R. Vértesi ¹³⁶, M. Verweij ⁵⁸, L. Vickovic ³³,
Z. Vilakazi¹²⁰, O. Villalobos Baillie ⁹⁹, A. Villani ²³, G. VINO ⁴⁹, A. Vinogradov ¹⁴⁰, T. Virgili ²⁸,
V. Vislavicius⁷⁴, A. Vodopyanov ¹⁴¹, B. Volkel ³², M.A. Völkl ⁹³, K. Voloshin¹⁴⁰, S.A. Voloshin ¹³⁴,
G. Volpe ³¹, B. von Haller ³², I. Vorobyev ⁹⁴, N. Vozniuk ¹⁴⁰, J. Vrláková ³⁷, C. Wang ³⁹, D. Wang³⁹,
Y. Wang ³⁹, A. Wegrzynek ³², F.T. Weiglhofer³⁸, S.C. Wenzel ³², J.P. Wessels ¹³⁵, S.L. Weyhmiller ¹³⁷,
J. Wiechula ⁶³, J. Wikne ¹⁹, G. Wilk ⁷⁸, J. Wilkinson ⁹⁶, G.A. Willems ¹³⁵, B. Windelband ⁹³,
M. Winn ¹²⁷, J.R. Wright ¹⁰⁷, W. Wu³⁹, Y. Wu ¹¹⁷, R. Xu ⁶, A. Yadav ⁴², A.K. Yadav ¹³²,
S. Yalcin ⁷¹, Y. Yamaguchi ⁹¹, S. Yang²⁰, S. Yano ⁹¹, Z. Yin ⁶, I.-K. Yoo ¹⁶, J.H. Yoon ⁵⁷, S. Yuan²⁰,
A. Yuncu ⁹³, V. Zaccolo ²³, C. Zampolli ³², F. Zanone ⁹³, N. Zardoshti ^{32,99}, A. Zarochentsev ¹⁴⁰,

P. Závada ⁶¹, N. Zaviyalov¹⁴⁰, M. Zhalov ¹⁴⁰, B. Zhang ⁶, L. Zhang ³⁹, S. Zhang ³⁹, X. Zhang ⁶,
 Y. Zhang¹¹⁷, Z. Zhang ⁶, M. Zhao ¹⁰, V. Zherebchevskii ¹⁴⁰, Y. Zhi¹⁰, D. Zhou ⁶, Y. Zhou ⁸²,
 J. Zhu ^{96,6}, Y. Zhu⁶, S.C. Zugravel ⁵⁵, N. Zurlo ^{131,54}

Affiliation Notes

^I Deceased

^{II} Also at: Max-Planck-Institut für Physik, Munich, Germany

^{III} Also at: Italian National Agency for New Technologies, Energy and Sustainable Economic Development (ENEA), Bologna, Italy

^{IV} Also at: Dipartimento DET del Politecnico di Torino, Turin, Italy

^V Also at: Department of Applied Physics, Aligarh Muslim University, Aligarh, India

^{VI} Also at: Institute of Theoretical Physics, University of Wrocław, Poland

^{VII} Also at: An institution covered by a cooperation agreement with CERN

Collaboration Institutes

¹ A.I. Alikhanyan National Science Laboratory (Yerevan Physics Institute) Foundation, Yerevan, Armenia

² AGH University of Krakow, Cracow, Poland

³ Bogolyubov Institute for Theoretical Physics, National Academy of Sciences of Ukraine, Kiev, Ukraine

⁴ Bose Institute, Department of Physics and Centre for Astroparticle Physics and Space Science (CAPSS), Kolkata, India

⁵ California Polytechnic State University, San Luis Obispo, California, United States

⁶ Central China Normal University, Wuhan, China

⁷ Centro de Aplicaciones Tecnológicas y Desarrollo Nuclear (CEADEN), Havana, Cuba

⁸ Centro de Investigación y de Estudios Avanzados (CINVESTAV), Mexico City and Mérida, Mexico

⁹ Chicago State University, Chicago, Illinois, United States

¹⁰ China Institute of Atomic Energy, Beijing, China

¹¹ Chungbuk National University, Cheongju, Republic of Korea

¹² Comenius University Bratislava, Faculty of Mathematics, Physics and Informatics, Bratislava, Slovak Republic

¹³ COMSATS University Islamabad, Islamabad, Pakistan

¹⁴ Creighton University, Omaha, Nebraska, United States

¹⁵ Department of Physics, Aligarh Muslim University, Aligarh, India

¹⁶ Department of Physics, Pusan National University, Pusan, Republic of Korea

¹⁷ Department of Physics, Sejong University, Seoul, Republic of Korea

¹⁸ Department of Physics, University of California, Berkeley, California, United States

¹⁹ Department of Physics, University of Oslo, Oslo, Norway

²⁰ Department of Physics and Technology, University of Bergen, Bergen, Norway

²¹ Dipartimento di Fisica, Università di Pavia, Pavia, Italy

²² Dipartimento di Fisica dell'Università and Sezione INFN, Cagliari, Italy

²³ Dipartimento di Fisica dell'Università and Sezione INFN, Trieste, Italy

²⁴ Dipartimento di Fisica dell'Università and Sezione INFN, Turin, Italy

²⁵ Dipartimento di Fisica e Astronomia dell'Università and Sezione INFN, Bologna, Italy

²⁶ Dipartimento di Fisica e Astronomia dell'Università and Sezione INFN, Catania, Italy

²⁷ Dipartimento di Fisica e Astronomia dell'Università and Sezione INFN, Padova, Italy

²⁸ Dipartimento di Fisica 'E.R. Caianiello' dell'Università and Gruppo Collegato INFN, Salerno, Italy

²⁹ Dipartimento DISAT del Politecnico and Sezione INFN, Turin, Italy

³⁰ Dipartimento di Scienze MIFT, Università di Messina, Messina, Italy

³¹ Dipartimento Interateneo di Fisica 'M. Merlin' and Sezione INFN, Bari, Italy

³² European Organization for Nuclear Research (CERN), Geneva, Switzerland

³³ Faculty of Electrical Engineering, Mechanical Engineering and Naval Architecture, University of Split, Split, Croatia

³⁴ Faculty of Engineering and Science, Western Norway University of Applied Sciences, Bergen, Norway

³⁵ Faculty of Nuclear Sciences and Physical Engineering, Czech Technical University in Prague, Prague, Czech Republic

³⁶ Faculty of Physics, Sofia University, Sofia, Bulgaria

- ³⁷ Faculty of Science, P.J. Safárik University, Kosice, Slovak Republic
³⁸ Frankfurt Institute for Advanced Studies, Johann Wolfgang Goethe-Universität Frankfurt, Frankfurt, Germany
³⁹ Fudan University, Shanghai, China
⁴⁰ Gangneung-Wonju National University, Gangneung, Republic of Korea
⁴¹ Gauhati University, Department of Physics, Guwahati, India
⁴² Helmholtz-Institut für Strahlen- und Kernphysik, Rheinische Friedrich-Wilhelms-Universität Bonn, Bonn, Germany
⁴³ Helsinki Institute of Physics (HIP), Helsinki, Finland
⁴⁴ High Energy Physics Group, Universidad Autónoma de Puebla, Puebla, Mexico
⁴⁵ Horia Hulubei National Institute of Physics and Nuclear Engineering, Bucharest, Romania
⁴⁶ Indian Institute of Technology Bombay (IIT), Mumbai, India
⁴⁷ Indian Institute of Technology Indore, Indore, India
⁴⁸ INFN, Laboratori Nazionali di Frascati, Frascati, Italy
⁴⁹ INFN, Sezione di Bari, Bari, Italy
⁵⁰ INFN, Sezione di Bologna, Bologna, Italy
⁵¹ INFN, Sezione di Cagliari, Cagliari, Italy
⁵² INFN, Sezione di Catania, Catania, Italy
⁵³ INFN, Sezione di Padova, Padova, Italy
⁵⁴ INFN, Sezione di Pavia, Pavia, Italy
⁵⁵ INFN, Sezione di Torino, Turin, Italy
⁵⁶ INFN, Sezione di Trieste, Trieste, Italy
⁵⁷ Inha University, Incheon, Republic of Korea
⁵⁸ Institute for Gravitational and Subatomic Physics (GRASP), Utrecht University/Nikhef, Utrecht, Netherlands
⁵⁹ Institute of Experimental Physics, Slovak Academy of Sciences, Kosice, Slovak Republic
⁶⁰ Institute of Physics, Homi Bhabha National Institute, Bhubaneswar, India
⁶¹ Institute of Physics of the Czech Academy of Sciences, Prague, Czech Republic
⁶² Institute of Space Science (ISS), Bucharest, Romania
⁶³ Institut für Kernphysik, Johann Wolfgang Goethe-Universität Frankfurt, Frankfurt, Germany
⁶⁴ Instituto de Ciencias Nucleares, Universidad Nacional Autónoma de México, Mexico City, Mexico
⁶⁵ Instituto de Física, Universidade Federal do Rio Grande do Sul (UFRGS), Porto Alegre, Brazil
⁶⁶ Instituto de Física, Universidad Nacional Autónoma de México, Mexico City, Mexico
⁶⁷ iThemba LABS, National Research Foundation, Somerset West, South Africa
⁶⁸ Jeonbuk National University, Jeonju, Republic of Korea
⁶⁹ Johann-Wolfgang-Goethe Universität Frankfurt Institut für Informatik, Fachbereich Informatik und Mathematik, Frankfurt, Germany
⁷⁰ Korea Institute of Science and Technology Information, Daejeon, Republic of Korea
⁷¹ KTO Karatay University, Konya, Turkey
⁷² Laboratoire de Physique Subatomique et de Cosmologie, Université Grenoble-Alpes, CNRS-IN2P3, Grenoble, France
⁷³ Lawrence Berkeley National Laboratory, Berkeley, California, United States
⁷⁴ Lund University Department of Physics, Division of Particle Physics, Lund, Sweden
⁷⁵ Nagasaki Institute of Applied Science, Nagasaki, Japan
⁷⁶ Nara Women's University (NWU), Nara, Japan
⁷⁷ National and Kapodistrian University of Athens, School of Science, Department of Physics, Athens, Greece
⁷⁸ National Centre for Nuclear Research, Warsaw, Poland
⁷⁹ National Institute of Science Education and Research, Homi Bhabha National Institute, Jatni, India
⁸⁰ National Nuclear Research Center, Baku, Azerbaijan
⁸¹ National Research and Innovation Agency - BRIN, Jakarta, Indonesia
⁸² Niels Bohr Institute, University of Copenhagen, Copenhagen, Denmark
⁸³ Nikhef, National institute for subatomic physics, Amsterdam, Netherlands
⁸⁴ Nuclear Physics Group, STFC Daresbury Laboratory, Daresbury, United Kingdom
⁸⁵ Nuclear Physics Institute of the Czech Academy of Sciences, Husinec-**Rez**, Czech Republic
⁸⁶ Oak Ridge National Laboratory, Oak Ridge, Tennessee, United States
⁸⁷ Ohio State University, Columbus, Ohio, United States
⁸⁸ Physics department, Faculty of science, University of Zagreb, Zagreb, Croatia
⁸⁹ Physics Department, Panjab University, Chandigarh, India

- ⁹⁰ Physics Department, University of Jammu, Jammu, India
- ⁹¹ Physics Program and International Institute for Sustainability with Knotted Chiral Meta Matter (SKCM2), Hiroshima University, Hiroshima, Japan
- ⁹² Physikalisches Institut, Eberhard-Karls-Universität Tübingen, Tübingen, Germany
- ⁹³ Physikalisches Institut, Ruprecht-Karls-Universität Heidelberg, Heidelberg, Germany
- ⁹⁴ Physik Department, Technische Universität München, Munich, Germany
- ⁹⁵ Politecnico di Bari and Sezione INFN, Bari, Italy
- ⁹⁶ Research Division and ExtreMe Matter Institute EMMI, GSI Helmholtzzentrum für Schwerionenforschung GmbH, Darmstadt, Germany
- ⁹⁷ Saga University, Saga, Japan
- ⁹⁸ Saha Institute of Nuclear Physics, Homi Bhabha National Institute, Kolkata, India
- ⁹⁹ School of Physics and Astronomy, University of Birmingham, Birmingham, United Kingdom
- ¹⁰⁰ Sección Física, Departamento de Ciencias, Pontificia Universidad Católica del Perú, Lima, Peru
- ¹⁰¹ Stefan Meyer Institut für Subatomare Physik (SMI), Vienna, Austria
- ¹⁰² SUBATECH, IMT Atlantique, Nantes Université, CNRS-IN2P3, Nantes, France
- ¹⁰³ Sungkyunkwan University, Suwon City, Republic of Korea
- ¹⁰⁴ Suranaree University of Technology, Nakhon Ratchasima, Thailand
- ¹⁰⁵ Technical University of Kosice, Kosice, Slovak Republic
- ¹⁰⁶ The Henryk Niewodniczanski Institute of Nuclear Physics, Polish Academy of Sciences, Cracow, Poland
- ¹⁰⁷ The University of Texas at Austin, Austin, Texas, United States
- ¹⁰⁸ Universidad Autónoma de Sinaloa, Culiacán, Mexico
- ¹⁰⁹ Universidade de São Paulo (USP), São Paulo, Brazil
- ¹¹⁰ Universidade Estadual de Campinas (UNICAMP), Campinas, Brazil
- ¹¹¹ Universidade Federal do ABC, Santo Andre, Brazil
- ¹¹² University of Cape Town, Cape Town, South Africa
- ¹¹³ University of Houston, Houston, Texas, United States
- ¹¹⁴ University of Jyväskylä, Jyväskylä, Finland
- ¹¹⁵ University of Kansas, Lawrence, Kansas, United States
- ¹¹⁶ University of Liverpool, Liverpool, United Kingdom
- ¹¹⁷ University of Science and Technology of China, Hefei, China
- ¹¹⁸ University of South-Eastern Norway, Kongsberg, Norway
- ¹¹⁹ University of Tennessee, Knoxville, Tennessee, United States
- ¹²⁰ University of the Witwatersrand, Johannesburg, South Africa
- ¹²¹ University of Tokyo, Tokyo, Japan
- ¹²² University of Tsukuba, Tsukuba, Japan
- ¹²³ University Politehnica of Bucharest, Bucharest, Romania
- ¹²⁴ Université Clermont Auvergne, CNRS/IN2P3, LPC, Clermont-Ferrand, France
- ¹²⁵ Université de Lyon, CNRS/IN2P3, Institut de Physique des 2 Infinis de Lyon, Lyon, France
- ¹²⁶ Université de Strasbourg, CNRS, IPHC UMR 7178, F-67000 Strasbourg, France, Strasbourg, France
- ¹²⁷ Université Paris-Saclay, Centre d'Etudes de Saclay (CEA), IRFU, Département de Physique Nucléaire (DPhN), Saclay, France
- ¹²⁸ Université Paris-Saclay, CNRS/IN2P3, IJCLab, Orsay, France
- ¹²⁹ Università degli Studi di Foggia, Foggia, Italy
- ¹³⁰ Università del Piemonte Orientale, Vercelli, Italy
- ¹³¹ Università di Brescia, Brescia, Italy
- ¹³² Variable Energy Cyclotron Centre, Homi Bhabha National Institute, Kolkata, India
- ¹³³ Warsaw University of Technology, Warsaw, Poland
- ¹³⁴ Wayne State University, Detroit, Michigan, United States
- ¹³⁵ Westfälische Wilhelms-Universität Münster, Institut für Kernphysik, Münster, Germany
- ¹³⁶ Wigner Research Centre for Physics, Budapest, Hungary
- ¹³⁷ Yale University, New Haven, Connecticut, United States
- ¹³⁸ Yonsei University, Seoul, Republic of Korea
- ¹³⁹ Zentrum für Technologie und Transfer (ZTT), Worms, Germany
- ¹⁴⁰ Affiliated with an institute covered by a cooperation agreement with CERN
- ¹⁴¹ Affiliated with an international laboratory covered by a cooperation agreement with CERN.